University of Copenhagen

A Master's Thesis

Building a Fluorescence Correlation Spectroscopy Setup

Author:
Ajmal Faizi

Supervisor:
Prof. Dr. Thomas Heimburg

February 20, 2015

Acknowledgments

First of all I want to thank Prof. Dr. Thomas Heimburg for allowing me to be a part of his group. I also offer my deepest gratitude and thanks to every member of the group especially Rima, Dievidas, Vardan, Lars, Karis and Alfredo for their kind words and encouragement in time when they were needed. I am also very grateful for the invaluable advice from Martin Gudman, Kasper Feldt and Axel Boisen. Last but not least I want to thank my family and dear friend Sharaz Butt for his unlimited support.

Abstract

This thesis gives a detailed description of how to construct a Fluorescence Correlation Spectroscopy (FCS) setup. FCS is a technique used for studying the dynamic characteristics of diffusing molecules in a solution. The setup consist of a laser ($532nm$, Nd:YAG max output power $50mW$), a telescope ($5mm-$ and $100mm$ lenses), a dichroic mirror cutoff $537nm$,a microscope objective ($60\times$W, NA 1.20, WD $0.25\mu m$), a clean up filter $542 - 622nm$, a pinhole ($100\mu m$, $50\mu m$, $30\mu m$), a detector (avalache photodiode (APD)) and a correlator card (FLEX5000/FAST). The detection volume of the setup is $\backsim 1.7fl$. The work presented here also concerns and treats some unexpected challenges in the form of ground loop formations connected with the construction of the setup. The newly constructed setup is then evaluated by conducting simple diffusion experiments on aqueous rhodamine 6G samples of varying viscosities by adding sucrose of differet $wt\%$s to the solution. The result show that the setup reacts as expected and it is capable of conducting diffusion measurements in aqueous solutions.

Contents

List of abbreviations

FCS	Fluorescence Correlation Spectroscopy
SMS	Single Molecule Spectroscopy
SM	Single Molecule
APD	Avalanche Photodiode
ACF	Auto-Correlation Function
CCF	Cross-Correlation Function
PCH	Photon Counting Histograms
FIDA	Fluorescence Intensity Distribution Analysis
NA	Nummerical Aperture
WD	Working Distance
OD	Optical Density
R6G	Rhodamine 6G
S/N	Signsl to Noise ratio
GL	Ground Loops

1 Introduction

Fluorescence Correlation Spectroscopy (FCS) is a well-known experimental technique that deciphers the dynamics of molecular events using statistical analysis of the temporal fluctuations occurring in a small observed volume (femtoliter). FCS has rapidly become a well established technique that facilitates investigation of a wide range of biophysical phenomena such as diffusion, binding processes, bacterial mobility, conformational changes in proteins etc. [1].

The idea of FCS was coined in the early 1970's. Magde *et al.* were the first to apply signal related correlation techniques experimentally to fluorescence in 1972 [6]. They are commonly credited as the "pioneers" of FCS. They along with Rigler *et al* a few years later published a series of important papers further establishing the theoretical foundation- and a variety of applications for FCS [7] [8] [9].

However, at the time, the technique was still not well developed and was poorly sensitive, partly because most of the required equipments for FCS were not widely applied in experimental settings of this nature. This was due to the relatively primitive technology. This resulted in the requirement for high concentrations of fluorescent molecules which made it difficult to conduct biological research. It was in the 1990's that FCS underwent its renaissance due to significant technological developments of it's main components. The availability of lasers with high beam quality and temporal stability, high quality microscope objectives with excellent imaging quality at high numerical aperture, and low noise single-photon detectors accompanied by the introduction of the confocal illumination scheme by Rigler *et al*

[10] consolidated FCS as a reliable tool single molecule spectroscopy (SMS). This lead to a number of technical improvements, making it possible to better define the measurement volume and achieve a better signal to noise ratio. This meant that interest in FCS was rekindled, since it now offered a much higher degree of sensitivity on a single molecule level. Today thousands of FCS related papers have been published and FCS has entered the industrial world with the introduction of a variety of commercial instruments used in biotech. research and in pharmaceutical-screening assays.

The main goal of the work presented here was to build a Fluorescence correlation Spectroscopy setup that would eventually be capable of preforming diffusion measurements on biological membranes. The setup was constructed mostly from optical components and electronic devices that were available and a few newly purchased parts. A test experiment was preformed to demonstrate the FCS setup's ability to preform diffusion measurements. This experiment demonstrate how the system reacts when the viscosity of an aqueous R6G solution with the same concentration is varied.

This thesis is written in a way, that it can be used as a guide for construction or realignment of FCS (or a partial guide for the construction of similar optical setups) setups. For this reason the methods section of this thesis gives a detailed description of the individual optical components and devices used and how each of them are incorporated in the system.

2 Theory

2.1 Fluorescence

In the past couple of decades there has been an incredible increase in the use of fluorescence in biological research. Fluorescence has become a profound methodology in biological sciences. This emphasis on the application of fluorescent dyes has gradually minimized the use of radioactive tracers for most biochemical measurements, which are expensive, more harmful to their environment and usually not as easy to work with [2].

Fluorescence is not a newly discovered phenomena. It was first observed and reported in 1564 by the Spanish scientist Nicolas Monardes. During the 19th. century the use of some fluorescent substances became popular. An interesting and well-documented example is from 1877, when fluorescein was added to the water of the Danube River in order to prove that it has an underground connection to the Rhine [2].

At present time, it is hard to imagine any biological research especially on a cellular level without the use of fluorophores, particularly when imaging processes are concerned. The flourophores ability to be easily detected has made fluorescence spectroscopy techniques primary research tools in biophysics and other biological research fields.

Fluorescence normally occurs from aromatic molecules called fluorophors [1]. Fluorescence can be described as the emission of light from substances that has been subjected to absorption of light, while a fluorophore is a molecule that can emit light when it is electronically exited [2].

[1] This thesis only deals with organic molecules i.e. fluorophores.

Fluorophores possess the unique ability to absorb and emit light of specific wavelengths. There are various types of fluorophores available commercially to choose from with different absorption and emission spectra.

In order to better understand how fluorescence occurs let's turn our attention to the Jabolanski diagram. This diagram was originally introduced by Alexander Jabolanki in 1935 to describe the absorption and emission of light. A standard Jablonski diagram (see figure 1) [2] is essentially an energy diagram that schematically illustrates the fluorescence activity.

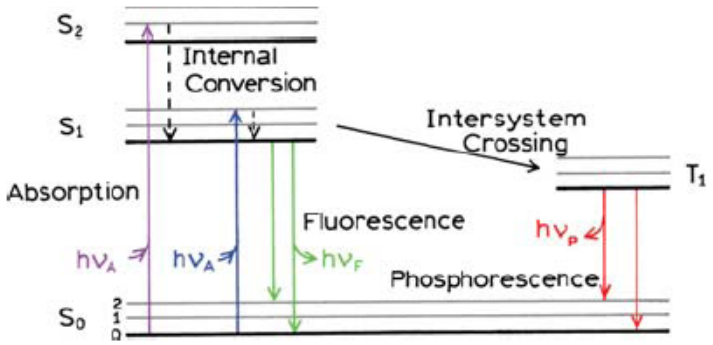

Figure 1: The Jablonski diagram: illustrating the transition between different energy levels of molecules. The ground state singlets and the singlet excited states are denoted as S_0i, S_1, S_2. 0, 1, 2 denotes the vibrational energy levels within each state. The above figure is a slightly modified version of [2] p.5.

The energy levels are arranged along the vertical axis, while along the horizontal axis the diagram is arranged into columns depicting specific spin multiplicities for specific species. The diagram depicts the singlet ground electronic state (the vertical parallel bars labeled S_0), the singlet 1st. electronic excited state S_1 and the 2nd. electronic excited state S_2. At each

[2]The above Jablosnki diagram is rather simple. A number of interactions such as quenching, energy transfer, and solvent interactions have been excluded.

of these energy levels the flourophore can exist in a number of additional vibrational energy levels illustrated as the multiple thinner lines denotes as $0, 1, 2$ and etc. at each electronic state. As the Jablonski diagram depicts, fluorescence occurs as the result of a three-stage process in the electron shells of fluorophores.These three stages can be described in the following manner:

- **Absorption**

  A photon of energy $h\nu_a$ supplied by an external source (i.e. a laser in this study) is absorbed by the fluorophore. This energy is used to pump an electron from the ground state S_0 to an excited state e.g. S_1 or S_2. This transitions occur in about $10^{-15}s$ [2].

- **Non-radiating transitions**

  Following absorption, several processes usually occur. The transition from S_2 to S_1 happens very quickly. The molecule loses energy due to e.g. internal vibrations. This process is known as internal conversion, which generally occurs within $10^{-12}s$ [2], and takes place prior to emission.

  The lifetime of the electron in the excited state is typically around $1-10$ns [2]. This is a decisive time. Since not only does the fluorophore experience conformational changes, but it can also undergo a number of possible interactions with its molecular environment e.g. collisions etc. These processes can affect how the relaxation from S_1 to S_0 occurs. The transition from S_1 to S_0 can occur via several different pathways.

  The transition can occur without the emission of a photon, since not all the molecules, which are initially excited by light absorption return to

S_0 by fluorescence. Several other processes such as collisional quenching, intersystem crossing (IC), fluorescence energy transfer (FRET) could also take place. The relaxation from S_1 to the ground state also occurs with fluorescence, if the energy of the initial S_1 substate partially dissipate, yielding a relaxed singlet excited state.

- **Fluorescence emission**

  The fluorophore returns to its ground state S_0 while emitting a photon of energy $h\nu_f$. Since the fluorophore experienced energy dissipation during the non-radiative relaxation (the excited state lifetime), the emitted photon would have less energy (longer wavelength) than the excitation photon of energy $h\nu_a$. This energy difference corresponds to the stokes shift (see figure 2), which is defined as the difference in wavelengths maximum- absorption and emission[2].

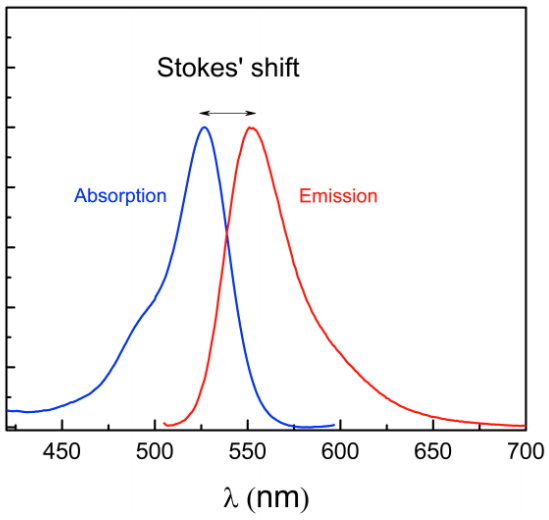

Figure 2: The graph shows the emission and absorption spectra of R6G, and the Stokes' shift. The above figure is a slightly modified version of [2] p.5.

FCS measurements requires fluorescence emitted by the sample under study which can either be natural e.g. green fluorescent protein (GFP) or from a labeling-dye. As discussed in latter sections the accuracy of FCS measurements depend among other factors on fluorescence emitted per molecule. Thus, there must be some basic requirements for the dyes used in FCS experiments. Dyes intended for FCS measurements should be characterized by:

- High extinction coefficient: corresponds to the probability that the dye will absorb a photon. This indicates that flourophores with higher extinction coefficient tend to emit more intensely and in return require less energy for their excitation.

- High fluorescent quantum yield: determines how much of the absorbed laser light will result in fluorescence. As mentioned earlier the transition from S_1 to S_0 can be either radiative or non-radiative. Since both scenarios are possible it is useful to define their ratio. This can be written as:

$$\phi_{fl} = \frac{k_{fl}}{k_{fl} + \sum k_{nr}} \tag{1}$$

  where ϕ_{fl} is the fluorescence quantum yield and k_{fl}, k_{nr} are rate constants for radiative and non-radiative transitions respectively.

- Low- singlet- to triplet state quantum yield and photobleaching: photobleaching is irreversible destruction of the flourophores. There is a certain probability that dyes in there excited state can be subjected to

photobleaching (see figure 3). However, this probability is not dependent on laser excitation intensities for weak intensity illuminations. For high intensity illuminations this relationship is very complicated since it includes "photobleaching" kinetics from several excited states[16].

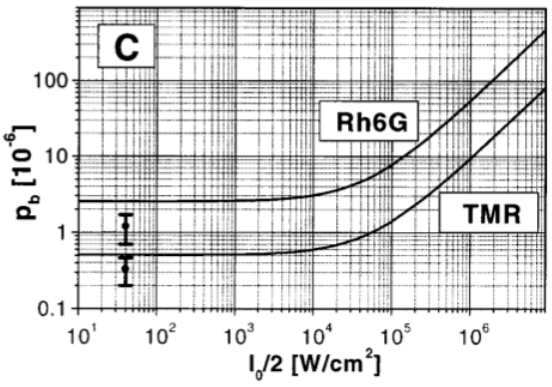

Figure 3: Dependency of the probability of photobleaching P_b of the dyes TMR and R6G on the excitation irradiance $I_0/2$. The above figure is from [16]

2.2 Diffusion

Diffusion was first observed by the English botanist Robert Brown in 1828. He observed pollen particles in water by using a microscope [3]. He noticed their erratic and irregular movements, which we know as Brownian motion.

However, it was Einstein that gave a quantitative explanation of the motion of Brownian particles in 1905 [5]. He showed that Brownian motions were caused by the impacts on the pollen particles by the even smaller (submicroscopic) water molecules. This conclusion was based on the fact that the water molecules because of their smaller size are more mobile than the the bigger pollen molecules. Therefor it is valid to assume that the pollen particles are being "kicked around" by the water molecules and not in reverse order. It is worth to mention that Einstein's analysis is also applicable to situations where the particles in the system are approximately the same size, or in other than liquid domains (gases and solids) as first studied by Brown.

However, this thesis is only concerned with the diffusion of particle in aqueous solutions, since the FCS setup is intended to be used for studying biological samples e.g. biological membranes.

Let's turn to the equations that quantitatively describe diffusion. Beginning by one of the most fundamental concepts of diffusion properties, first formulated by Adolf Fick in 1855. Fick derived his first- and second law based on simple assumptions, which are the following differential equations [4].

$$J_x = -D\frac{\partial C}{\partial\, x} \tag{2}$$

$$\frac{\partial C}{\partial t} = D\frac{\partial^2 C}{\partial x^2} \tag{3}$$

Fick's first law eq. 2 describes the steady state flux J_x of the particles which is induced by the concentration gradient $\frac{\partial C}{\partial x}$. D is the diffusion coefficient, and has the units m^2/s and relates to how far a particle can can move due to its diffusive motion. C is the concentration of the particles and x is the one-dimensional space coordinate.

Fick's second law eq. 3 states how the concentration varies over time. Actually Einstein in his paper [5] looked at Fick's second law from a statistical perspective and re-introduced it. The numerical solution to this equation describes the mean squared displacement (MSD) $\langle x^2 \rangle$ of the diffusive particle in one dimension. MSD describes the area that the particle covers in a certain time.

$$\langle x^2 \rangle = 2 \cdot D \cdot t \tag{4}$$

This solution is obviously only applicable when the observation time is longer than the diffusion time of the individual particles. The above equation in two- and three dimensions can be given in terms of $\langle r^2 \rangle$. In two dimensions, the square of the distance from the origin to the point (x, y), is $r^2 = x^2 + y^2$, therefore

$$\langle r^2 \rangle = 4 \cdot D \cdot t \tag{5}$$

In three dimension, $r^2 = x^2 + y^2 + z^2$ thus

$$\langle r^2 \rangle = 6 \cdot D \cdot t \tag{6}$$

This relation displays linearity between the mean square of the translation distance of a particle and time. This statement can be verified by following the trajectory of a single particle over time, or by averaging the diffusion paths of many particles. By using Fick's first law in combination with Stoke's law Einstein derived the famous diffusion equation also known as the Stokes-Einstein equation for macroscopic spheres in liquid solutions.

$$D = \frac{k_B T}{f} = \frac{k_B T}{6\pi\eta R_H} \tag{7}$$

where k_B is the Boltzmann constant, T is the absolute temperature, f is the friction coefficient, η is the viscosity of the solution, and R_H is the hydrodynamic radius of the particle.

The basic concepts of diffusion described above only apply to diffusion in homogeneous and continuous systems. However, artificial- and biological membranes are not necessarily homogeneous. Therefor diffusion in biological membranes is a complex process and can depend on many different factors. These factors can be due to domain- and raft formations, which can cause local variations of the viscosity of the lipid matrix. This will have a significant effect on the diffusion of both lipids and proteins.

2.3 The Mathematical Basis

FCS is a statistical method, which analyzes the fluctuations in fluorescence signals. These fluctuations typically originate from Brownian motions of the dye- or dye labeled molecules through a small confocal volume, which is basically a small laser spot (see figure 4). The size of these molecules determines the mean time they spend within the confocal volume [3]. A very sensitive detector i.e. avalanche photodiode(s) (APD) records single photons emitted by the dye molecules in the confocal volume, which results is an intensity trace representing random noise (see figure 4). The relevant information about the dynamics of the system such as diffusion time, size, number of particles and concentration can be extracted by using correlation functions that convert random noise into correlation curves (see figure 4).

There are different varieties of correlation functions. In cases where only one type of fluorescent dye and one detector are used, the auto-correlation method can be applied. In other cases where the sample contains one or two dyes and two detectors are used, a method called cross-correlation can be used [4]. The FCS-setup described here only consists of one APD, and the test experiments conducted only contain one type of fluorescent dye. Therefore this section will only deal with auto-correlation. Cross correlation shall be explained and discussed in discussion section.

[3] for example if a small, dye tagged molecule binds to another and perhaps bigger molecule, it slows down and emits photons for a longer period of time during its diffusion through the laser spot

[4] Other common methods to use fluorescence fluctuations to probe molecular interactions include Photon Counting Histograms (PCH) and Fluorescence Intensity Distribution Analysis (FIDA). Coincidence Analysis is used to probe rare events in the femto-molar range.

2.3.1 Basic Correlation Function

Since the size of the confocal volume is very small (in order of femtoliters), there will be considerable fluctuations in the fluorescent signal. Therefore it is likely that at any given time there might be one or several fluorescent molecules present at the small detection volume accompanied by background noise. The fluorescent signal is typically recorded by illuminating the tiny confocal volume(see figure4 5), in order to detect single particles, which are diffusing through the the observation volume. The FCS-setup described in this thesis has an assumed 3D Gaussian and ellipsoidal shaped observation volume with a radius of ??? and a length of ???.

The diffusing fluorescent molecule(s) in the focus absorbs laser light, which results in the excitation of the molecule to a higher energy level (figure 1). After a characterestic time (e. g. $3.9ns$ for Rhodamine 6G[2]) the fluorophor will emit light of a different wavelength, resulting in returning the molecule to it's ground state. These emitted bursts of light contribute to the fluorescent signal.

The fluorescent signal can be separated from the background noise by using correlating functions in the intensity of the fluorescent light emitted from discrete molecules.

The horizontal line (see figure 4c) indicates the level of background fluorescence as well as the ground level of the intensity. The peaks are due to the bursts of emitted light from the fluorophores diffusing through the confocal volume. The sizes of the peaks are related to the concentrations of the fluorescent molecules as well as their trajectory through the focus.

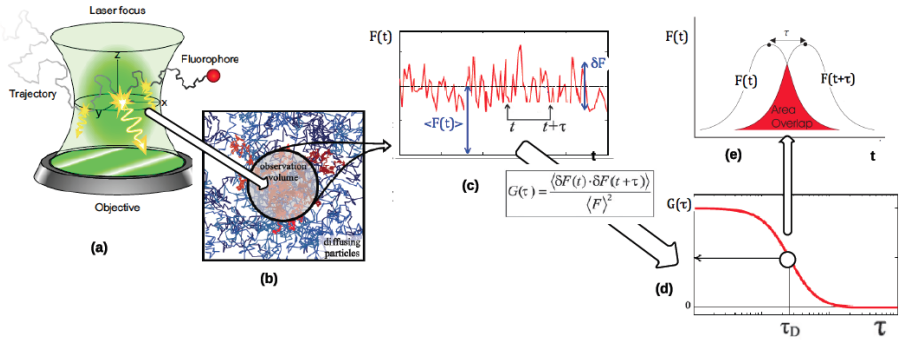

Figure 4: An illustration of the detection and correlation of the fluorescent signal. (a) illustrates the ellipsoidal Gaussian volume. (b) shows the illuminated part of the sample. (c) the trace of the fluorescent signal. (d) the correlation function. (e) the overlap area between the fluorescent signal $F(t)$ and it's delayed form $F(t+\tau)$ corresponding to the characteristic diffusion time. Figure 4a is from [18] p. 29.

The intensity as a function of time can be written as:

$$F(t) = \langle F(t) \rangle + \delta F(t) \tag{8}$$

where $\langle F(t) \rangle$ is the average intensity over time and $\delta F(t)$ is the fluctuation of the intensity at time t.

Auto-correlation mathematics, which are one of the most powerful tools for noise reduction was actually introduced by Weiner [11] almost two decades before the development of the FCS.

The auto-correlation function facilitates the transformation of data from the measured time- [5] to the correlation time domain[6]. In essence, the aut-correlation function is a measure of the self similarity of a signal $F(t)$ be-

[5] how long it take to acquire the data.

[6] how fast the fluctuations take place, e.g. how long a molecule stays in the confocal volume

longing to the emission of discrete molecules. In other words, the recorded intensity at time t is correlated with that recorded at time $t + \tau$. If the intensity of the signal has not changed considerably in the specified period of time (i.e. if there is no time-shift) the correlation is high. On the other hand if the signal is completely different (i.e. large time-shift) the correlation is low. One can therefor also think of the correlation function is a "memory" function that measures how long a signal stays the same over a specified time interval. The correlation function $G(\tau)$ is defined as:

$$G(\tau) \equiv \frac{\langle F(t) \cdot F(t+\tau) \rangle}{\langle F(t) \rangle^2} \tag{9}$$

The correlation of the fluorescence intensity $F(t)$ is quite similar to correlating fluorescent light intensity fluctuations $\delta F(T)$.

$$G(\tau) \equiv \frac{\langle \delta F(t) \cdot \delta F(t+\tau) \rangle}{\langle F(t) \rangle^2} \tag{10}$$

The only difference between eq. 9 and eq. 10 is an additive constant -1. $\delta F(T)$ contains the information about the measured fluctuations. The constant term (constant offset) $\langle F(t) \rangle$ can only reduce the signal. Therefore it is important to note that increasing $\delta F(T)$ reduces the measurement volume and decreasing $\langle F(t) \rangle$ reduces background noise.

Essentially three important pieces information can be extracted from the correlation function:

- the average number of fluorescent particles $\langle N \rangle$ in the detection volume.
- the size of the confocal volume (r_0, z_0) (which can for example be found by conducting Rhodamine R6G reference measurements).

- the average time it takes for a molecule to move through the confocal volume τ_D, and the translational diffusion coefficient D_τ.

For further analysis it is necessary to express the correlation function in terms of $\langle N \rangle$, τ_D, r_0, and z_0 The fluorescent intensity $F(t)$ is assumed to be proportion to physical quantities such as [2]:

- q, the detection quantum efficiency
- σ_{abs}, the excitation cross section of the fluorescent particles
- ϕ_f, the fluorescent quantum yield
- $CEF(\overrightarrow{r})$, the collection efficiency function. It can be defined as the fraction of emitted fluorescence at a given position $\overrightarrow{r}$, which passes the pinhole on the way to the detector(s) [10].
- $I(\overrightarrow{r})$, the excitation intensity at position $\overrightarrow{r}$.
- $C(\overrightarrow{r}, t)$, signifies the concentration of fluorescent particles at position $\overrightarrow{r}$ and time t.

and thus $F(t)$ can be written as:

$$F(t) = q \cdot \sigma_{abs} \cdot \phi_f \int_v CEF(\overrightarrow{r}) \cdot I(\overrightarrow{r}) \cdot C(\overrightarrow{r}, t) dr^3 \tag{11}$$

rewritting the equation,$Q = \sigma_{abs} \cdot \phi_f$ and $I_{em} = CEF(\overrightarrow{r}) \cdot I(\overrightarrow{r})$ yields:

$$F(t) = q \cdot Q \int_v I_{em}(\overrightarrow{r}) \cdot C(\overrightarrow{r}, t) dr^3 \tag{12}$$

Since fluorescence intensity fluctuation $\delta F(t)$ can be expressed in terms of concentration fluctuations $\delta C(\overrightarrow{r},t) = C(\overrightarrow{r},t) - \langle C \rangle$ rewriting once more for the fluorescence light intensity fluctuations $\delta F(t)$ yields:

$$\delta F(t) = q \cdot Q \int_v I_{em}(\overrightarrow{r}) \cdot \delta C(\overrightarrow{r},t) dr^3 \tag{13}$$

substituting eq. 13 and 12 into eq. 10 gives:

$$G(\tau) = \frac{\int_v \int_{v'} I_{em}(\overrightarrow{r}) \cdot I_{em}(\overrightarrow{r'}) \cdot \langle \delta C(\overrightarrow{r},t) \cdot \delta C(\overrightarrow{r},t+\tau) \rangle dr^3 dr'^3}{(\int_v I_{em}(\overrightarrow{r}) \cdot \delta C(\overrightarrow{r},t) dr^3)^2} \tag{14}$$

by applying Fick's second law of diffusion:

$$\frac{d}{dt}\delta C(\overrightarrow{r},t) = D_\tau \cdot \bigtriangledown^2 \delta C(\overrightarrow{r},t) \tag{15}$$

which explains the space-time dependency of the concentration fluctuations $\delta C(\overrightarrow{r},t)$ one obtains the "concentration correlation function":

$$\langle \delta C(\overrightarrow{r},t) \cdot \delta C(\overrightarrow{r},t+\tau) \rangle = \frac{\langle C \rangle}{(4\pi D_\tau \tau)^{\frac{3}{2}}} \cdot exp\left(\frac{-(\overrightarrow{r} - \overrightarrow{r'})^2}{4D_\tau \tau}\right) \tag{16}$$

assuming that the detection efficiency profile is 3D and Gaussian both along the axial and radial directions:

$$I_{em}(x,y,z) = q \cdot Q \cdot I_0 \cdot exp\left(-2\frac{x^2+y^2}{r_0^2}\right) \cdot exp\left(-\frac{2z}{z_0^2}\right) \tag{17}$$

where r_0 and z_0 are respectively the radial and axial distances from the

center of the focus (see figure 5), while x and y denotes coordinates in the central plane of the focus.

The standard Gaussian assumption has been the subject of debate since it has been shown that it might not be accurate under some common experimental conditions (see 2.3.2)

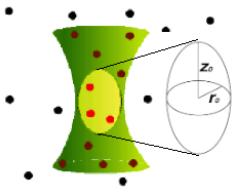

Figure 5: An illustration of the ellipsoidal and Gaussian confocal volume .

However, continuing under the standard assumption that the observation volume is ellipsoidal, and Gaussian, the correlation function for the freely diffusion particles in aqueous solution [7]can be easily obtained by substituting eq. 16 and 17 into eq. 14 and solving numerically:

$$G(\tau)_{3D} = \frac{1}{\langle N \rangle} \cdot \left(\frac{1}{1 + \frac{\tau}{\tau_D}} \right) \cdot \left(\frac{1}{1 + \sqrt{1 + \frac{r_0^2 \cdot \tau}{z_0^2 \cdot \tau_D}}} \right) \tag{18}$$

where τ_D is the characteristic diffusion time i.e. the time that the fluorescent dye spends at the detection volume of radius r_0 and the length z_0 (usually around $1\mu m$). τ_D can be expressed in terms of r_0 and D_τ as:

$$\tau_D = \frac{r_0^2}{4D_\tau} \tag{19}$$

[7]in the absence of chemical kinetics.

the mean number of particles in the detection volume can be given as:

$$\langle N \rangle = V_{det} \cdot \langle C \rangle \tag{20}$$

here V_{det} is the detection volume and can be written as $V_{det} = \pi^{\frac{4}{3}} r_0^2 z_0$ [18]. Both $\langle N \rangle$ and τ_D can be obtained from eq. 18. As $\langle N \rangle$ (at concentration $\langle C \rangle$) is simply $G(0) = \frac{1}{\langle N \rangle}$ i.e. the amplitude of the correlation graph in a certain detection volume and τ_D is the value if τ corresponding to the half amplitude of the correlation function.

However, for FCS measurements of membranes (as apposed to freely diffusing rhodamine 6G in water) a 2D version of eq. 18 is needed. Since the diffusion of a dye molecule in the membrane should be treated in 2D because lipid membranes have a thickness of about approximately $5nm$ which is much smaller than the axial length of the detection volume $\backsim 1\mu m$. This allows for the re-writing of eq. 18 in the analytical form:

$$G(\tau)_{2D} = \frac{1}{\langle N \rangle} \cdot \left(\frac{1}{1 + \frac{\tau}{\tau_D}} \right) \tag{21}$$

2.3.2 The standard assumption of the detection volume being Gaussian

The above analysis (and the curve fitting procedure) assumes a 3D Gaussian detection volume. It is important to mention that this approximation is only good for small pinholes. Some studies like Hess et al.[12, 13] have shown that standard assumption of the 3D detection volume being Gaussian is not entirely an accurate approximation under many common measurement conditions.

These deviations are common sources of systematic errors and manifest themselves in the correlation curve as an additional exponential component. According to the above mentioned studies theses deviation can have a severe impact on the measured diffusion times as they can be shifted by as much as $\backsim 80\%$.

However, these studies also offer suggestions that can either eliminate or at least reduce the artifacts to a negligible level in order to achieve a nearly Gaussian detection volume. Hess et al. suggested the following measures:

- a smaller detector aperture.
- underfilling $< 60\%$ the objective back aperture .
- using two photon excitation.
- correcting the auto-correlation function for the additional exponential component.

2.3.3 The signal to Noise ratio (S/N)

As mentioned earlier the rate of fluorescence- emission and detection is proportional to the average number of $\langle N \rangle$ molecules in the detection volume. This implies that for large $\langle N \rangle$ (i.e. high concentrations) the background noise will be smaller hence better accumulated photon statistics.

However, it was also established that the amplitude of the correlation function is inversely proportional to $\langle N \rangle$. This means that the signal itself will be large for lower $\langle N \rangle$ (i.e. smaller concentrations). This arises a key question. Is an optimal concentration needed to obtain the most accurate FCS data?

The issue of statistics in FCS measurements was first investigated by Koppel [23]. Koppel concluded that the two above mentioned effects actually exactly cancel each other out for a wide variety of concentrations. Furthermore, he concluded that the signal to noise ratio S/N is dependent on the rate of photon detection per fluorescent molecule (i.e. particle brightness and correlator bin size), and independent of the sample concentration. S/N can be expressed as a function of $G(\tau)$ and the variance of $G(\tau)$ [23]:

$$S/N = \frac{G(\tau)}{\sqrt{var\ G(\tau)}} \tag{22}$$

There are primarily two factors that causes fluctuations $\delta n(t)$ in the number of detected photons per sampling time.These factors are:

- fluctuations in the number of fluorescent particles N in the detection volume e.g. due to diffusion etc. As mentioned above these fluctuations affect both the signal $G(\tau)$ and the noise $\sqrt{var(G(\tau)}$. In this case the fluctuations in the number of fluorescent particles N is related to the relative fluctuations in photon counts:

$$\frac{\sqrt{var\ \delta N}}{\langle N \rangle} = \frac{1}{\sqrt{\langle N \rangle}} \tag{23}$$

- fluctuations in the number of detected photons per fluorescent particle. Since this type of fluctuations at different time intervals are not correlated, they only affect the noise. These are called 'Poisson noise' or 'shot noise' and are due to fluctuations in the random emission of photons from 'fixed' fluorescent molecules.

Since this type of noise depends on the total number of detected photons it's relative value can be given as [23]:

$$\frac{\sqrt{var\ \delta n(t)}}{\langle n \rangle} = \frac{1}{\sqrt{\langle n \rangle}} = \frac{1}{\sqrt{\nu \langle N \rangle}} \tag{24}$$

here, ν is the mean number of detected photons per fluorophore per sampling time interval. The value of ν is typically small for most FCS measurements [24] [23]. Shot noise is uncorrelated. For large $\langle N \rangle$ and for small ν it dominates the 'total' noise $\sqrt{var\ G(\tau)}$. This means that the signal to noise ratio given in equation 22 can be expressed as:

$$S/N = \frac{G(\tau)}{\sqrt{var\ G(\tau)}} \approx G(\tau)\ \nu\ \langle N \rangle\ \sqrt{T} \tag{25}$$

where, ν is the mean number of detected photons per fluorophore per sampling time interval and T is the total of accumulated sampling time intervals Δt. $T\Delta t$ is then the total duration of the experiment. The above equation shows that S/N depends on $\nu\sqrt{T}$ [8].

Two important conclusions can be drawn from the above discussion and especially equation 25.

For large $\langle N \rangle$ the FCS statistics are only dependent on the photon count rate per fluorophore and the total acquisition time. There is no dependence on the number of fluorophores per detection volume. In addition at very low concentrations, S/N is proportional to $1/\sqrt{\langle N \rangle}$. FCS measurements are mostly reliable at concentrations in the $1nM$ - $1\mu M$ range. At this regime,

[8] keeping in mind that $G(\tau) \propto \frac{1}{\langle N \rangle}$

S/N is essentially independent of the number of fluorophores in the detection volume [23].

The dependency of S/N is stronger on ν than T. This emphasizes the extremely importance of optimization of the photon detection in the experiment.

3 Material and Methods

3.1 Constructing a Fluorescence Correlation Spectroscopy setup

As mentioned in the introduction the goal of this thesis is to construct and test a FCS setup that can investigate diffusion processes in biological membranes. This section shall provide a detailed explanation of the construction process of the setup. As follows from the theory section, the requirements for conducting FCS measurements are mainly:

- a small detection volume in order to ensure very low number of particles at the volume. Hence, a correlation function with a high amplitude.
- high efficiency of photon detection, that leads to a good rejection of the background fluorescence.

Both of these requirments can be meet perfectly by building a confocal FCS setup [10].

The FCS setup in our laboratory was initially constructed by a former PhD-student, A. Hac, as a part her PhD dissertation [17] and for the related articles [22] and [21].

Later on the setup has been modified and partially rebuilt a number of times by different people who were working on the setup at the time.

The initial goal of this project was to make the existing setup work by the simple realignment of the light path from the laser to the APDs.

However, after spending months trying to make the setup work with out a successful outcome it was decided to completely rebuild the setup from

scratch. Several components of the setup were under suspicion of malfunction or defect.

The setup was eventually completely taken apart including the table and all the components. Each component was individually taken apart, cleaned, fixed, tested and reassembled. Only a new correlator card, a $5mm$ lens and a clean up filter were purchased. The rest of the components and parts constituting the setup are from the previous setup(s). However, the setup still did not produce correlation curves. So the alignment processes was repeated many times until multiple ground loops were detected. These ground loops were an insidious source of severe ground loop related noise problem. This problem was very irregular as it appeared and disappeared totally unexpected making the electronic devises act erratic and unpredictable. Diagnosis, and tracking the source(s) of ground loops were a very tedious, time consuming and difficult task. The nature of ground loops along with tracking and removing them is explained in the discussion section.

3.1.1 An Overview of the setup

The setup (see figures 6 and 7) is based on the confocal principle (more detailed descriptions of the individual components are given in Appendix B). An incident $532nm$ laser beam from a Nd:YAG $50mW$ laser, running in TEM_{00} mode is expanded and collimated to $7.2mm$ using a telescope consisting of two lenses with respective focal lengths of $5mm$ and $100mm$ expanding the beam 20 times. The expanded laser beam slightly overfills the $7mm$ back aperture of the water immersion objective N.A. 1.2. Between beam expander and objective the laser beam is passing through optical den-

sity filters (in a rotateable holder) lowering the laser power by various factors (i.e. OD $3, 2, 1, 0.6, 0.2$ and 0) in order to reduce photobleaching (see figure 3) as much as possible. Lowering of laser power is crucial for fulfilling the criteria needed for the assumption of a Gaussian excitation intensity distribution [13]. Next, the laser beam is directed towards the microscope objective through the dichroic mirror (cut-off $537nm$) by a reflective mirror in the stage.

The laser focus is located within the sample in order to excite the fluorescent molecules passing through the detection volume. Part of the fluorescence light emitted by the fluorescent molecules during their trajectory through the detection volume is then collected by the aforementioned microscope objective.

Any residual laser excitation light (stray and Rayleigh scattering from the fluorescent particles and water) along with Raman-scattered light from water molecules are removed by cleanup filter (Transmission $542 - 622nm$).

An avalanche photodiode APD (Laser Components GMBH, SPCM-AQR-13) operating in photon counting mode (Geiger mode) is placed behind the pinhole (rotating disk $100\mu m$, $50\mu m$, $30\mu m$). The diameter and position of the pinhole are chosen in a way that fluorescent light coming from near the focal spot was transmitted through the pinhole in the image plan while the remaining out-of-focus light from outside the observation volume is strongly attenuated (confocal detection). Next, the in-focus signal is recorded by a single APD. The output of the APD is time auto-correlated using a hardware correlator card (Correlator.com, Flex5000, Bridgewater, NY, USA).

Initially, it was planed to incorporate two APDs in the setup by dividing

(50 : 50) the signal after the pinhole by using a polarising beam splitter. However, this was not possible due to one of the available APDs not working properly. This results in the inability to record in cross-correlation mode. The differences between using one- or two APDs is discussed in detail in the discussion section.

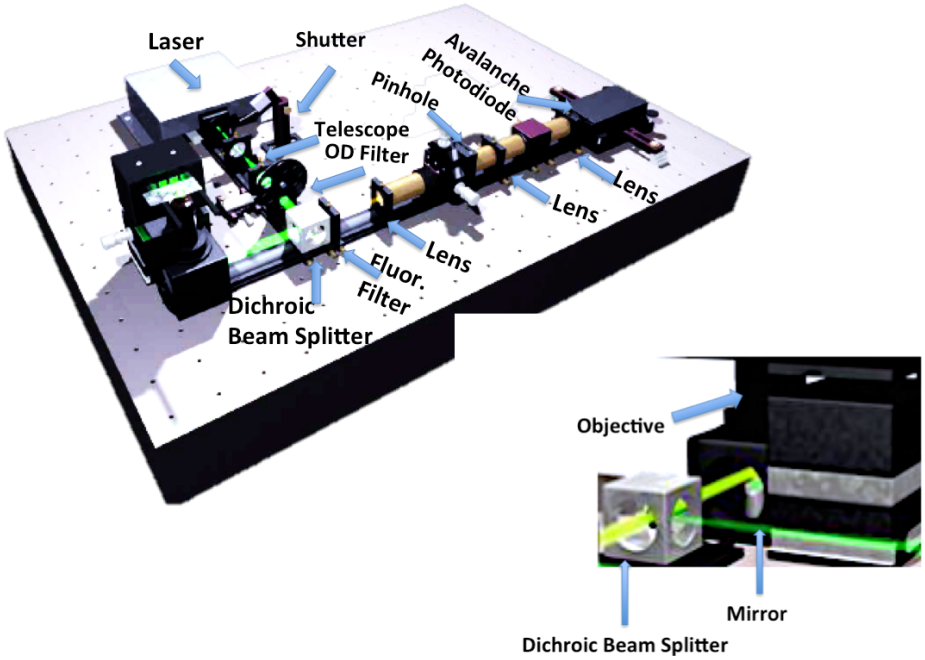

Figure 6: **Left**: An overview of the setup. The green light is the excitation laser beam while the orange light is the fluorescent signal emitted by the sample. The figure is a modified version of [19]. **Right**: A view of the stage from another angle showing the propagation of the excitation and fluorescent light. The figure is a modified version of [18] p. 40.

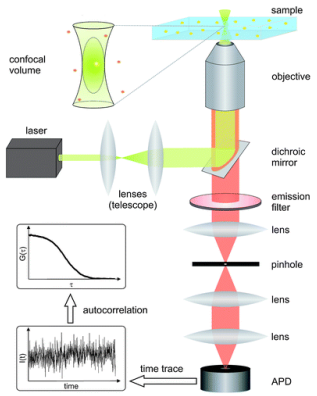

Figure 7: A sketch of the FCS setup. Figure from [29]

3.1.2 The optical table

The dimensions of the table are $100 \times 130cm$. The optical table is considered as a very important part of the setup. Since its stability and ability to be shock absorbent is fundamental, not only in the construction phase but also in the future when the setup is constructed and in use. The more stability the table provides the less/minor adjustments and realignments shall the setup require.

The first logical step is to make sure that the table is completely horizontal and as shock absorbent as possible [9]. The shock absorbency of this particular table mostly depends on the material it stands on as oppose to newer models that have several shock absorbent mechanisms built in the table it self.

Before the alignment process the table is taken apart cleaned, oiled and reassembled[10].

[9] FCS is not extremely sensitive to vibrations as opposed to for example optical tweezers, since the stability of their traps depends among other things on the shock absorbency of the table

[10] this was done since the height adjustable mechanism of the table was not in working order.

It is very important to make sure that the table is positioned as horizontally as possible. A spirit level is used to measure the slope of the table at least at four different positions on the table. All optical tables are usually height adjustable at each leg. The height of every leg of the table is adjusted until the spirit level at different positions displays complete horizontality.

3.1.3 Laying the tracks

After the table is completely horizontal, the tracks for the optical axis are laid. The tracks constitute the back bone of the setup. It is a good idea to position them in a way, that reaching to different parts of the setup is easy during the alignment process at the construction phase and also for future optimization of the different parts of the setup. The tracks were laid in a "L" (see figure 6) shape. It is vital that the tracks are completely parallel to the edges of the table. The tracks are then secured with screws. The next step is mounting the laser.

3.1.4 The excitation source

The choice of lasers as the excitation sources for FCS setups is based on the required excitation wavelengths of the type(s) of fluorophores, which are intended to be used in the experiments.

Today, a wide variety of dyes are commercially available, but typical dyes chosen for FCS experiments have absorption bands in the blue-green region of the electromagnetic spectrum [24]. This is Probably due to the availability of low cost lasers, which have wavelengths in that particular region of the spectrum. These lasers have typically argon ion (wavelengths $\backsim 488-514nm$)

and Nd:YAG (wavelength $\backsim 532nm$) gain media. They provide a stable and controllable excitation light, and typically produce polarized and collimated beams with Gaussian intensity profiles (see figure 8).

The laser (CW, $532nm$, max output power $50mW$, beam diameter $0.36mm$ and running in TEM_{00} mode) chosen for the setup was already available in the lab. As mentioned earlier, the choice of laser depends mostly on which dye(s) are planned to be used in the experiments. Normally, once the laser is decided upon finding an appropriate dye(s) should be easy and vice versa.

However, there are also a few other properties besides the wavelength of the laser that should be carefully considered. Since they play an important role in defining the laser excitation in confocal setups.

- **Max. ouput power of the laser:**

  Excitation of the dyes can be achieved by one- or multi-photon [11] approach. The setup described in this thesis is based on the one-photon approach, which is suitable for most fluorophores that are available commercially. Typically continuous wave (CW) lasers with output powers in order of a few miliwatts are used in such systems [24].

  The dye emission should be in the linear range of its dependence on the laser excitation. This is not possible if the intensity of the excitation is too high. Higher laser powers results in a number of photophysical events including triplet excitation and photobleaching (see figure 3) that affects the accuracy of FCS data to a great extent [17][16].

[11] very high laser intensities are required in order to achieve multi-photon absorption. This can usually be achieved by using short pulse lasers (such as titanuim sapphire lasers) combined with high numerical aperture objectives.

However, OD-filters can help to to apply the minimum laser power possible (greatest attenuation) while still obtaining a good fluorescence signal.

- **The intensity profile of the beam:**

  The intensity profile of the beam should be Gaussian (see figure 8) i.e. the laser should be running in TEM_{00}- mode[12]. This type of intensity profile is needed since the illuminated spot should be a volume with a Gaussian intensity profile in the image plane (x,y-plane), while the intensity profile along the optical axis (z-axis) is assumed to be Gaussian 2.3.2.

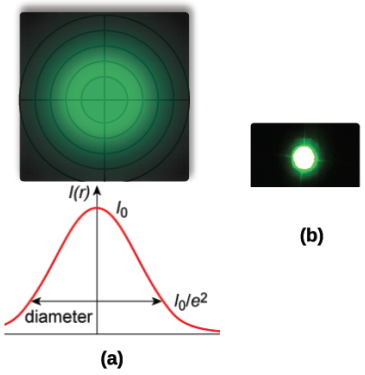

Figure 8: **left**: an illustration of the Gaussian profile of a laser spot. The graph shows how intensity drops towards the edges. **Right**: an actual picture of the beam as it leaves the telescope and hits the wall of the lab. The cross seen in the picture is due to the beams passage through a crosshair which was placed in continuation of the telescope.

[12] TEM_{00} Transverse Electromagnetic Modes which means that the beam has neither electric nor magnetic field in the direction of propagation. This mode is typically denoted as TEM_{pl}, where p and l are integers indicating the radial and angular mode orders, respectively. When $p = l = 0$, the TEM_{00} mode is the lowest order, and has the same form as a Gaussian beam.

- **the diameter of the laser beam:**

  knowing the exact output diameter of the beam is also important as the beam is typically expanded and kept collimated by a telescope or beam expander. The choice of the telescope lenses depend partly on the diameter of the laser beam.

Aligning the Laser:

the laser beam constitutes the optical axis of the setup, which should pass through the exact center of all lenses and other optical components of the setup. Aligning the laser beam can be a very tedious and challenging task if it is not done carefully and in a systematic manner. It is obviously absolutely vital to be familiar with the safety rules and regulations when working with lasers, since stray light can be very hazardous. Therefor it is strongly advised to be very cautious during the alignment process. It is worth mentioning that usually it is preferable to use less powerful lasers when constructing FCS setups for safety (and practical) reasons, even though optical density filter can be applied to reduce the beam intensity. When working with powerful lasers even a reflection from ones finger nail could be potentially dangerous. So in addition to using less powerful lasers one should always use the correct laser safety eyeware and always look down at the beam from a standing position. Avoiding being in the plane of laser propagation direction reduces the risk of being exposed to reflections considerably. The laser was mounted in the following manner:

- After the laser is placed loosely at its chosen position (see figure6). A precision pinhole is placed opposite of the laser at the farthest point on the track. A cardboard target (piece of cardboard paper) is placed

behind a precision pinhole (a widely used tool in laser alignment procedures). The laser beam is then carefully steered into the precision pinhole. When the laser spot is propagating through the pinhole aperture and the observed spot is at its brightest the laser is secured with four screw at each corner of the laser. Careful positioning the screws on the laser and gentle tightening are required for fine-tune adjustments.

- Next, a second precision pinhole is placed between the laser and the first precision pinhole which was placed at the previous step. This time the laser beam is steered in a way that it propagated through both precision pinholes simultaneously, while keeping an eye on the intensity of the laser spot (on the cardboard target as in previous step). The vertical position of the beam is controlled by tightening the screws while the horizontal position is determined by moving the laser very carefully sideways.

- The above step is repeated many times while varying the positions of the two precision pinholes on the track until the beam is completely parallel independent of the respective varying positions of the two pinholes on the track between the laser and the cardboard target.

The following step is widening and collimating the beam by constructing a telescope. However, first, it is important to reduce the laser intensity for the construction of the rest of the setup in order to reduce the risk of stray light related accidents.

3.1.5 Optical Density (OD) Filters

A rotateable neutral filter holder with five different OD-filters is placed in front of the laser in order to control the power of the laser beam. The neutral filters have the following optical densities (0.1, 0.6, 1, 2, 3). During the construction process of the setup a second holder is placed after the telescope to provide a series of choices for the power of the beam (see figure 6) in order to reduce the laser power for safety reasons. Optical density can be expressed as a function of the transmittance[17]:

$$OD = log_{10}(1/T) = log_{10}\frac{Initial\ intensity}{Intensity\ after\ OD\ filter} \tag{26}$$

The above expression can be used to calculate the laser powers when different OD filters are implemented.

Filter /OD	calculated laser power/mW
0	5
0.1	3.97
0.6	1.26
1	0.5
2	0.05
3	0.005

However, the calculated laser powers are not the same as actual laser powers due to loss of intensity of the beam to the different optical components. Several measurements of the laser excitation power P conducted at different points in time measured by a power meter (Thorlabs PM100A) showed that actual power after the microscope objective is approximately $55-65\%$ of the

calculated values (see the above table). The output power was measured to be $5.05mW$.

The loss of laser power at the objective is partially due to the reflection by the surface of lenses and other components, and some is lost because of it's imperfect transmission through lenses (e.g. due to absorption at coating- and glues material of the encountered components).

Dust and dirt also reduce the intensity. Therefore it is important to keep the setup clean from dust using pressurized filtered air. It is also important to be familiar with how to handle lenses and other optical components that includes glass, lenses etc in order to avoid contamination.

Furthermore, the actual power at the sample is even lower still due to losses at the coverslip and water interfaces.

By knowing the actual laser power one can try to keep photo bleaching at minimum level. The level of photobleaching has been determined according to Eggeling [16] as shown in figure 3. The calculated radius r_0 of the laser focus from rhodamine 6G measurements can be used a long with the laser power P to calculate the focal excitation irradiance $I_0/2$:

$$\frac{I_0}{2} = \frac{P}{\pi r_0^2} \tag{27}$$

Different fluorophores have of course different levels of photobleaching as shown for rhodamine 6G and TMR in figure 3.

3.1.6 The telescope

Prior to the construction of the setup, it is important to decide upon which components (lenses, pinhole, mirrors and bandpas filter(s)) should be used.

These decisions are typically based on several factors such as the wavelength- and diameter of the laser beam, the type and numerical aperture of the objective, the dimensions of the detector-opening, and also the path lengths from the laser to the objective and from the objective to the detector(s).

Constructing the telescope

For the alignment of the setup a widened and parallel (collimated) beam is required. Since usually the beam diameter leaving the laser is about $\backsim$ 0.2-2mm (the diameter of the laser used in our setup is 0.36mm). The collimation and expansion of the beam diameter can be achieved by a telescope.

A telescope can be constructed of two lenses which have different focal lengths. The distance between the two lenses is adjusted in a way that the focal point of the first lens (of shorter focal length) coincides with the focal length of the second lens (of longer focal length)(see figure 9). Once this is achieved a collimated beam of the desired diameter can be obtained.

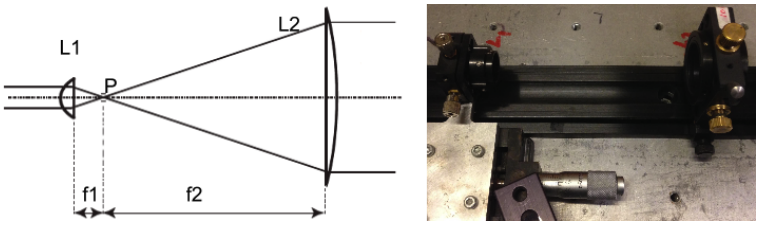

Figure 9: **Left**: an illustration of the telescope consisting of two lenses of different focal lengths. **Right:**: actual picture of the telescope made of two lenses with respective focal lengths of 5mm and 100mm

Usually when the correct distance between the two lenses is found the beam will be focused to the focal point P (see figure 9). The focal lengths of the two lenses define the expansion ratio of the beam. To achieve best

results plano-convex lenses can be used and oriented as shown in the above picture.

However, first, it is necessary to calculate the focal lengths of the lenses needed for the construction of the telescope.

The back focal plane of the objective[13] is $7.2mm$ (see 3.1.9). The diameter of the beam as it exits the laser is $0.36mm$. This means that the diameter of the laser beam has to be expanded 20 times so it fills (or slightly overfills) the back focal plane of the objective. The respective focal lengths of the two lenses can be calculated as follows:

$$focal\ lenght\ of lens\ 1 = \frac{0.36mm}{7.2mm} \cdot focal\ lenght\ of lens\ 2 \qquad (28)$$

Based on the above calculation lenses of focal lengths $5mm$ (L_1) and $100mm$ (L_2) are chosen.

The construction and alignment of the laser beam through the telescope is achieved by the following systematic procedure:

1. The $5mm$ lens (L_1) is mounted on a micrometer adjustable (in the light propagation direction) bench (see figure 6). The micrometer-wise adjustablity of the position of (L_1) plays a very important role in the optimization of the setup later in the construction process.

2. First, the L_1-micrometer complex is placed on the first track ($\backsim 16cm$ away from the laser) and secured well with screws to the table.

3. The next step is to make sure that the laser beam propagates through

[13] corresponding to diameter of the incoming laser beam into the back of the objective

the exact center of the $5mm$ lens. To achieve this two precision pinholes are placed on the track at each side of the lens.

At this point the beam passes very well through the first precision pinhole and it is steered into the second precision pinhole by L_1 with gentle adjustments of the lens-holder-screws. These adjustments are continued until the beam propagates through both precision pinholes (while propagating through the exact center of L_1).

To make sure that the beam propagates perfectly through both precision pinholes (and through L_1) a cardboard target is placed after the second pinhole (in the direction of beam propagation) to make sure that the laser spot is at brightest[14].

For fine adjustments the distances of the precision pinholes from L_1 are varied and the procedure is repeated several times.

4. The other lens of the telescope L_2 is placed ($\backsim 11.5cm$)[15] in continuation of L_1 in the beam propagation direction and secured (loosely at first) in order to expand the beam diameter 20 times to $\backsim 7.2mm$.

   The alignment of the beam through L_2 is done in the same manner as for L_1 with two precision pinholes and a cardboard target.

5. Step 3 and 4 are repeated several times to make sure that the beam propagates through the exact center of both lenses.

   After making sure that the beam diameter is approximately the re-

[14] since the beam has a Gaussian profile. This would mean that the exact center of the beam is getting through the pinholes and L_1 (see figure 8)

[15] at this distance the diameter of the beam is roughly $\backsim 7.2mm$

quired size. It is made sure by repeatedly checking that the beam leaving the telescope is propagating completely straight.

Since the beam diameter is quite bigger after the telescope and compared to the precision pinhole size ($\backsim 100\mu m$) the above procedure is repeated in exact same manner. This time with precision double pinholes where the beam is steered to propagate perfectly through both of the openings of the double precision pinholes while keeping an eye on the intensity of the laser spot on the cardboard target.

6. It is important to continuously check the collimation of the beam leaving the telescope. The more collimated the beam is the less it will diverge as it propagates.

   FCS requires highly collimated[16] beam of an appropriate diameter in order to obtain a small confocal volume (see figure 4).

   The collimation of the beam is checked by measuring the beam diameter after passing through the telescope at several positions along the propagation direction.

   Next, the opening of an iris aperture is closed down repeatedly to certain various diameters, all shorter than $7.2mm$. The iris aperture is positioned in the beam propagation direction after the telescope. A cardboard target depicting a cross hair and marked for the diameters corresponding to the various chosen diameters of the iris aperture opening is placed repeatedly at several positions along the beam propagation

[16]It is not possible to achieve a perfectly collimated beam, with no divergence due to diffraction.

to check whether the beam diameter diverges. L_2 is moved back and forth accordingly until no divergence of the diameter can be observed.

7. Auto-collimation is performed for fine adjustments and control. A cardboard target is placed a few mm off-axis from the focal point of L_1 ($5mm$). A mirror is held after L_2 in the propagation direction. The incoming beam from the telescope is reflected back through L_2 on the cardboard target. The position of L_2 is adjusted until the laser spot observed on the cardboard target is as focused as possible.

   Typically when as focused laser spot as possible is obtained by this method, it means that approximately the correct distance between the two telescope lenses (i.e. in this case L_1 and L_2) is found. This corresponds to the fact that the focal point of L_1 coincided with the focal length of L_2 (see figure 9).

8. After the installation of the stage the collimation of the beam is further optimized by a using a cross hair as shown in figure 10. It is mounted instead of the microscope objective on the stage. Here very fine adjustments are made by carefully adjusting the micrometer-screw (on the micrometer adjustable bench (see figure 9)) until the pattern shown in the figure below is observed on the selling of the setup.

   However, as seen in the picture above the observed pattern is not a perfect "cross hair-pattern". But only this pattern resulted in a correlation curve every time.

   Theoretically a perfect cross hair-pattern indicates that the focal point of L_1 coincides with the focal length of L_2 which in turn corresponds

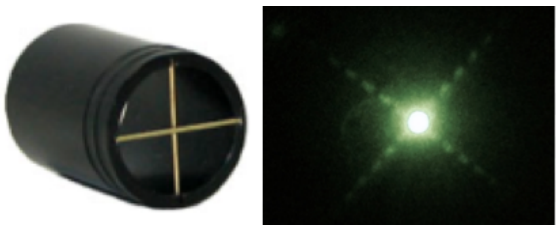

Figure 10: **Left**: A cross hair that can be placed instead of the microscope objective for optical alignment purposes. Right: The actual pattern obtained by using the cross hair that eventually resulted in a obtaining the correlation curve.

to a well-collimated beam (see figure 9). This irregularity can possibly be explained by arguing that there might be either imperfections in the optical components, imperfect alignment or both.

The next step is the instillation of the dichroic mirror so that the light leaving the telescope can be directed towards the reflective mirror which in turn reflects the beam into the back of the objective. The dichroic mirror also transmits the fluorescence light towards the detector.

3.1.7 The dichroic mirror

The dichoric mirror reflects laser light $< 537nm$ coming from the telescope and directs it towards the reflective mirror in the stage that in turn directs the beam into the back of the microscope objective.

The dichoric mirror also transmits the fluorescent light $> 537nm$ emitted by the sample through the objective towards APD through the pinhole (see figure 11).

The dichroic beamspliter glass plate is installed and secured (by glue) in a holder (see figure 6) that tilts it at an angle towards the stage.

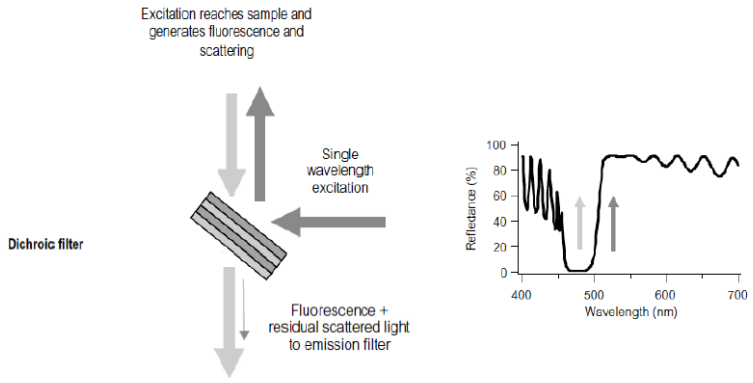

Figure 11: An illustration of the principle of dichroic mirror. The excitation light is reflected towards the objective and the fluorescence (and residual scattered excitaion light) from the sample is transmitted through. The figure is a modified version of [24] p. 123.

The alignment process of the dichoric mirror can be divided into two step i.e. the alignment of the incident laser light reflected - and the fluorescent light transmitted by the dichroic mirror respectively.

Alignment of the incident laser light reflected by the dichroic mirror

- The dichoric mirror is placed loosely on the second track opposite to the telescope. The vertical position of the beam parallel to the table is controlled by carefully sliding the dichroic mirror up and down the track.

- Fine adjustments are made by putting two precision pinholes respectively in front (between the telescope and the dichroic mirror) and after the dichroic mirror (between the dichoric mirror and the stage) (see figure 6).

- A cardboard target is placed after the second precision pinhole in the light propagation direction. The position of the dichroic mirror is slightly varied while making sure that the light propagated through both precision pinholes while keeping an eye on the cardboard target for the brightest light spot possible. When the light passes perfectly through both precision pinholes and the brightest possible spot is observed on the cardboard target, the dichroic mirror is very carefully secured by its screws to the track. Tightening these screws dramatically alters the alignment, therefor caution is advised for future optimization.

- The above step is repeated several times while varying the respective positions of the two precision pinholes (precision double pinholes were also used) while keeping an eye on the intensity of laser spot on the cardboard target.

Alignment of the transmitted fluorescent light through the dichroic mirror

Once the reflective mirror inside the stage is installed and correctly positioned (see section 3.1.8) the dichroic mirror is aligned for fluorescent light emitted by the sample through the objective and reflected by the mirror inside the stage toward the dichroic mirror.

For the alignment of the fluorescent light the water- objective is used and a concentrated sample of R6G ($10\mu M$) is prepared (R6G at $10\mu M$, OD 2 produces a bright beam of fluorescent light that was suitable for aligning). The alignment is preformed by two precision pinholes in the following manner:

- Each of the two precision pinholes are placed in front and after the dichroic mirror respectively in the propagation direction of the fluorescent light. A cardboard target is placed after the second precision pinhole. The fluorescent light is then steered to pass through both precision pinholes while observing the intensity of the fluorescent light spot on a cardboard target. Adjustments are only made by changing the position of the dichroic mirror with extreme care and caution, since even tightening/loosing the screw of the dichroic mirror alters the position of the beam to an extreme extent.

- The above step is repeated several times while the positions of the two precision pinholes are varied.

3.1.8 The stage complex and the reflective mirror

The stage complex (see figure 6) consists of a reflected mirror, $x-, y, z$-nanopositioning system and an opening for the microscope objective.

Mounting the stage complex

Prior to adjusting the reflective mirror, it is important to make sure that the stage complex is positioned and mounted correctly on the table.

The correct mounting of the stage is achieved by placing a spirit level on top of the stage during the mounting process. If the stage is not completely mounted parallel to the table then the microscope objective would not be positioned entirely perpendicular to the table. This would potentially make the alignment process very difficult or perhaps even impossible. After stage

complex is installed correctly, it is secured by screws to the table. Its position relative to the table is rechecked by a spirit level.

Adjusting the reflective mirror

The reflective mirror is glued to an angle-adjustable part of the stage. This part resembles a "lever arm" that rotates the mirror in vertical- and horizontal direction. This movement is controlled by three adjustable screws at the back of the stage. The vertical- and horizontal rotation of the mirror is used for centering the beam at the back of the microscope objective.

In order to center the beam and make it propagate exactly perpendicular to the table the objective is replaced with the cross hair (see figure 10). Since centering a wide beam in the cross hair proved to be complicated, first an iris aperture (it diameter reduced to $\backsim 1mm$) is placed after the dichroic mirror (between the dichroic mirror and the stage complex). This results in the reduction of the laser spot diameter to a point-like spot which can be observed on the cross hair.

Next, the point like laser spot is steered into the middle of the cross hair by the three adjusting screws, which control the position of the mirror (i.e. the position of the spot in the cross hair). When centering the laser spot in the cross hair is achieved the mirror is at the correct desired position.

3.1.9 The microscope objective

The microscope objective is probably the single most crucial parts of FCS-setups. They are basically compound lenses, made of several individual mobile collaborative parts (see figure 12).

In FCS setups, objectives are critical for the generation of small detection volumes as well as collection of the fluorescence from the sample. Thus, the requirements must be high- transmission and light collection efficiency as aberration free as possible.

Possible inherent optical aberrations in the objective can alter the measurements severely e.g. by increasing the size of the detection volume (i.e. enlargement of focal spot size), changing the distribution of light at the focus (i.e. deviating from Gaussian profile) etc.

Luckily, high N.A. microscope objectives, which are available commercially are typically corrected to a great extent for optical aberrations (infinity corrected, i.e. that image plane is at infinity).

The suitability of the microscope objectives for FCS measurements can be assessed primarily by considering the following properties of an objective: the numerical aperture NA , magnification, the working distance WD and how corrected they are for optical aberrations.

In the setup described in this thesis, the objective is pointing upwards (inverted) and the propagation of light to and from the sample goes through a thin coverglass. This means that the medium between the objective and the coverglass is air. Due to the refraction at the air-glass interference the numerical aperture is limited to ~ 1.

An objective with high NA meets therefore all the requirements mentioned above. Since FCS requires efficient- fluorescence collection and transmission, high power objectives (NA > 1, and long WD) are ideal.

The NA of an objective describes the half collection angle over which the collection of light occurs through the lens. The half collection angle can be

obtained from Snell's law.

$$NA = n \cdot sin(\alpha_{objec}) \tag{29}$$

where, n is the refractive index of intervening media. For air n= 1, water n=1.33 and for microscope immersion oil n=1.52. The NA of an objective can have a significant effect on its light collection efficiency.

α_{objec} is the half collection angle. The light collection efficiency of an objective η_{objec} can be expressed in terms of the half collection angle given by the following equation[17] [2]:

$$\eta_{objec} = \frac{1}{2} \cdot (1 - cos(\alpha_{objec})) \tag{30}$$

For example NAs 0.6, 1.2 and 1.45 respectively corresponds to η_{objec}'s $\sim 10\%$,$\sim 29\%$ and $\sim 40\%$ of the total sphere of collection around the detected particle . This suggests that NA can have a significant effect on the light collection efficiency of the objective.

However, it must be noted that objectives perform to their best capability when implemented under the right conditions. For example in diffusion experiments in aqueous solutions the implementation of oil-immersion (high NA) objectives would not be very effective. Since in aqueous solutions the molecules which are being measured are normally not in contact with the coverglass. In this kind of samples the location of the detection volume is usually chosen to be several μm deep into the sample. This is done in order to minimize possible artifacts which are due to particles being attached

[17] normalized for 4π

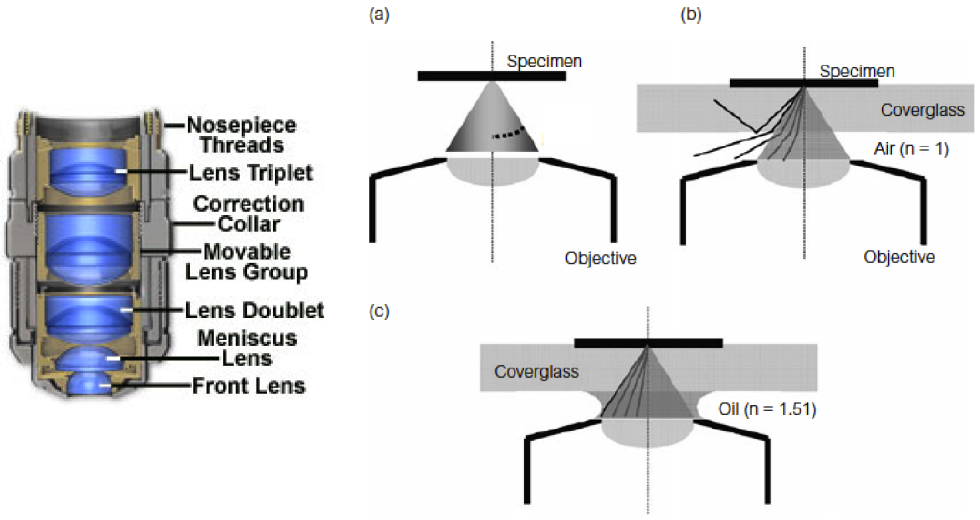

Figure 12: **Left**: An illustration of the anatomy of a microscope objective. The figure is from (www.olympusmicro.com). **Right**: a) Illustration of a microscope objective showing that the numerical aperture NA of an objective is defined by the half angle of the cone of rays. b) and c) Illustrates how immersion oil effects the cone of rays when working through a coverglass both when the space between the coverglass and objective is filled with air or oil. The figure is from [24]. p. 128.

to the surface of the coverslip. In this case the NA would be limited to a value close to the refractive index of the solvent in which the sample is dissolved (for example water ~ 1.33). Measurements where the molecules under study are located some distance into an aqueous solution usually require the implementation of water immersion objectives. Under these conditions the performance of water immersion objectives is not compromised as opposed to oil immersion objectives.

Oil-immersion objectives are usually not well suited for most FCS experiments since they tend to focus and collect light in environments with high

refractive indices namely the immersion oil and the coverglass. This means that the oil-immersion objectives are most efficient when focusing and gathering light just at the surface of the cover glass. If laser light is focused a few microns deeper (from the glass-water interface) into a sample in aqueous solution it would result in optical aberrations and poor fluorescence collection.

The chosen water-immersion objective for our setup is a standard Olympus objective. The tube lens focal length $180mm$ (UPLAPO, $60\times$, NA 1.2 , WD $0.25mm$,F.N 26.5, C.C.$0.13 - 0.21\mu m$, objective focal length $3m$). The objective focal length ($\frac{tube\ lens\ focal\ length}{magnification}$) is $3mm$. The diameter of the back focal plane ($2 \cdot NA \cdot objective\ focal\ length$) is $7.2mm$. The objective focal length and the diameter of the back focal plane are need to calculate the focal lengths of the two lenses of the telescope (see3.1.6).

Installation and alignment of the microscope objective

Before the objective is placed in the stage it was made sure that the incident laser beam is well aligned. The cross hair-objective (see figure 10) is placed instead of the microscope objective and two precision pinholes are placed in the incident beam path. This results in reducing the size of laser light spot to a easily controllable tiny spot. The three adjusting screws of the reflective mirror in the stage are used to steer the tiny light spot to the exact middle of the cross hair.

Next, the precision pinholes are removed and the intensity profile of the beam is checked by observing it on the ceiling of the setup.

Afterwards the microscope objective is placed in the stage (replacing the cross hair objective).

As mentioned earlier FCS is sensitive to optical aberrations and arti-

facts generated from surface absorption effect (particularly in free diffusion measurements). Optical aberrations in fluorescent solutions with various refractive indices gradually occurs as the depth of the focusing of the excitation light increases.

It is therefor necessary to use adaptive optical elements in the construction of the setups. Here correct- adjustment of the correction collar and focusing are important.

Focusing: As mentioned earlier it is highly important to avoid the impact of artifacts generated by surface absorption effects. FCS measurements in aqueous solution requires that the detection volume is placed at repeatable distances deep into the sample. It is also important that the size and profile of the detection volume is reproducible

However, as the overview of the setup shows (see figure 6) and (see figure 7) the setup does not include a CCD camera or any other form of binocular observation of the sample.

Incorporation of a CCD camera into the setup should be relatively easy and beside using it for focusing, it could also be used for supplementary microscopy studies.

However, in the current design routine focusing is achieved by an "observation mirror". The observation mirror is a flip-glass placed in the excitation-light propagation direction after the telescope. It simultaneously allows the transmission of the excitation light and its reflection from the coverglass. Quick focusing is done by placing (i.e. by flipping) the observation mirror in the excitation light path and observing the diffraction pattern of the reflected excitation light. The flip-mirror is removed from the light path while

performing FCS measurements.

3.1.10 The band-pass filter

The samples used for the FCS measurements are in aqueous solutions. This presents a big problem regarding the unwanted contribution of the water molecules in the sample to the background noise. If these contributions are not filtered out, one would face the problem of having a relatively large background signal from the water molecules. These molecules are superior in numbers compared to the single dye molecules of interest. Simple calculations reveal that in $0.1fl$ of water there are $\backsim 10^9$ water molecules [24]. If even a fraction of the these molecules make unwanted contributions to the signal overlapping the spectral region of the single dye single molecule the S/N would be far from ideal. It should also be noted that in addition, S/N is usually also influenced by complications with the instrumentation such as stablity of the laser beam, mechanical drift, detector- afterpulsning and dead time, and detector non-linearity.

However, there are mainly two sources of these unwanted contributions:

- Raman scattering by the water-molecules: contributes photons at both higher and lower wavelengths compared to the laser excitation light (Anti-Stokes at $443 - 455nm$ and Stokes $639 - 665nm$) [24].

- Rayleigh scattering by the water-molecules: These scatterings contributes to the background signal at the excitation wavelengths.

Raman scattering which is mainly light at longer wavelengths should be the main concern. Since the emitted light from the dye molecule would also

be of longer wavelength.

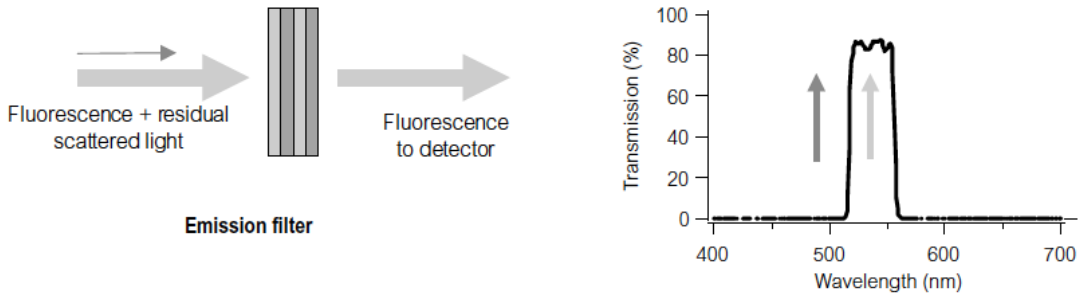

Figure 13: An illustraion of the principle of the emission filter. The filter removes most of the remaining excitation scattered- and unwanted fluorescence light. The figure is a modified version of [24]. p. 118.

To minimize these unwanted contributions to the signal an emission filter that transmits $542-642nm$ is placed after the dichroic beamsplitter (between the dichroic beamsplitter and the L_3 lens) (see figure 6). The choice of these filters should of course be in accordance with the emission spectrum of the dye 2. This filter blocks scattered laser light (at the excitation wavelengths). It also minimizes the effects of Raman scattered- and Rayleigh scattered light from the water molecules in the detection volume.

However, Some of the above mentioned Stokes scattered photons might overlap the filter pass band and pass through to the detector. The band pass filter can not totally block all of the Rayleigh scattering.

However, in order to minimize these unwanted contributions to the signal to a larger degree two different band pass filters could be used. This was successfully done by [17].

3.1.11 The Pinhole

After the collected fluorescence is filtered by the bandpass filter it reaches L_3 (plano-convex, focal length $140mm$), which focuses the light to a diffraction limited spot. Precisely at this focus the pinhole (a rotating circular disk consisting of three different pinholes $100\mu m$, $50\mu m$ and $30\mu m$) is placed.

The fluorescence light propagating through the pinhole will have a near-Gaussian intensity profile, if the pinhole is matched with L_3 to the size of the diffraction limited light beam. The radius of the focused light spot r_0 perpendicular to the direction of propagation can be expressed as [25]:

$$r_0 = \frac{1.27\lambda f}{nD} \tag{31}$$

where λ is the wavelength of the laser, f is the focal length of the objective, n is the refractive index of the medium where the light is focused and D is the diameter of the beam.

However, here it is important to keep in mind that this value relates to a theoretical minimum. Due to different sorts of optical aberrations present in the optical system it is challenging to reach this limit. Typically the diameter of these focal spots are ranging from $\backsim 500nm$ to $1\mu m$ [24]

The next component i.e. L_4 (plano-convex, focal length $140mm$) merely collimates the diverging beam producing a near-Gaussian beam and directs it towards L_5 and the detector 6.

Considerations for the Pinhole Size

The confocal detection scheme requires a narrow pinhole in the optical detection path. As described above the collected fluorescence light by the objective is focused onto the pinhole in a way that only light collected from very close to the focal plane of the objective is transmitted through the pinhole (see figure 15). So the L_3-pinhole-L_4 system functions as a 'spatial-filter', as its purpose is to define as close to a near-Gaussian profile as technically possible. The pinhole is of course an extremely important element of the setup as it defines the confocal volume and prevents the unwanted artifacts[18] from reaching the detector.

The confocal scheme should be constructed in a way that, it efficiently reduces the detection volume. The detection volume is achieved by the rejection of the light emitted from regions away from the focal plane of the objective, which will be out of focus at the pinhole (see figure 15). This out of focus light will therefor not reach the detector.

Rigler *et al* [10] were the first to theoretically and experimentally investigate the effects of pinhole size on the S/N ratio. Pinhole Sizes corresponding to the image of the beam waist at the plane of the pinhole resulted in the best S/N ratios. Depending on the objective usually pinhole sizes $30 - 100um$ are used [17] [10].

However, it has to be mentioned that pinhole sizes in order of $250\mu m$ have been used in some studies [19] like (Eggeling *et al* 1998)[16].

In accordence with these findings pinhole sizes corresponding to an airy

[18] artifacts arising for example from scattering by dirt particles on the laser output lens or as result of undesirable transverse modes etc.

[19] where the detection volumes have been bigger compare to the usual setups.

disc (focal diameter of an objective) can be calculated as follows:

$$diameter\ of\ pinhole = Magnification{\cdot}diameter\ airy\ disc = 60{\cdot}0.541\mu m = 33\mu m \tag{32}$$

the focal diameter of the objective can be calculated by:

$$\frac{1.22 \cdot \lambda_{laser}}{NA} = \frac{1.22 \cdot 532nm}{1.2} = 0.541\mu m \tag{33}$$

The pinhole diameter should also be in accordance with the focal lengths of L_4 and L_5 (see figure 15). This is very important because the size of the pinhole image (i.e. diameter of the fluorescent beam as it leaves the L_4 towards the detector) should be focused on the active area of the detector which is very small. The dimensions of the active area of the APD are $176\mu m \times 176\mu m$. The pinhole image diameter can be calculated as:

$$image\ diameter = pinhole\ diameter\ \times\ \frac{focal\ length\ of\ APD\ lens}{focal\ length\ of\ pinhole\ lens} \tag{34}$$

the pinhole lenses have the focal length $140mm$ and the lens chosen for the APD i.e. L_5 has a focal length of $\backsim 100mm$. According to the above equation the image diameter is $71.4\mu m$. Similar calculations of the image for $50\mu m$ and $30\mu m$ gives $35,7\mu m$ and $21,4\mu m$ respectively.

Alignment of the pinhole lenses L_3 and L_4

Prior to the aligning of the pinhole the two pinhole- lenses L_3 and L_4 ($140mm$ each)(see figure 6) were first aligned without the pinhole.

The procedure of the alignment of the two lenses is very similar to that of the telescope. The main difference is that here we are not interested in widening the beam but only focusing it onto the pinhole by L_3 and collecting and collimating the "clean" Gaussian beam after the pinhole by L_4 (see figure 14).

- Laser light is used for the alignment. A reflective 90 mirror is placed instead of the dichroic mirror. This mirror reflects laser light towards the L_3-L_4 complex which is used for alignment and collimation. The alignment and collimation of the beam (without the pinhole) is done by precision pins and by auto-collimation described in step 7. 3.1.6.

- The above procedure is repeated but now with a strong R6G sample after the re-installment of the dichroic mirror [20].

Alignment of the pinhole

The alignment of the pinhole along with the construction of the telescope are the most vital and challenging steps of the FCS construction process. The three different size pinholes are located on a circular disc, which is incorporated in a z,y-z micrometer adjustable mechanical system (see figure 6). After the correct installment of the two pinhole-lenses the pinhole is placed precisely at the focus (see figure 14).

[20] the active area of the APD is covered when the detector is not in use in order to avoid

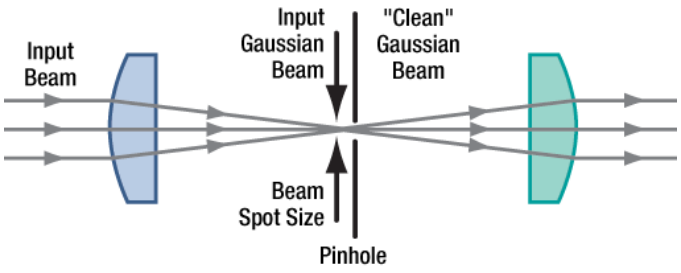

Figure 14: An illustration of the "spatial filter" consisting of a lens-pin-lens system. The lenses are both plano-convex of focal lengths 140mm. This system provides an as near-Gaussian beam profile as practically possible. The is from Thorlabs tutorial, principles of spacial filter (www.Thorlabs.de).

However, at this point it is absolutely important that the light all the way from the laser to L_4 is well-aligned and collimated.

The alignment for the pinhole is basically done in two steps by observation and by detection i.e. with- and without the use of APD.

- *Without APD*: first $100\mu m$ pinhole is chosen. The three x-,y and z micrometer-screws controlling the position of the pinhole are used to place the pinhole precisely at the focus (see figure 14) . A card is held after the pinhole (in front and behind L_4) in the light (from a concentrated R6G sample) propagation direction to check the shape and intensity of the beam. Next, Two precision pins are placed in front and behind the pinhole to make sure that the alignment is as precise as possible. The light is guided through both precision pins and the pinhole (by careful adjustment of the micrometer-screws) while checking the light spot size and intensity on a card. The above procedure is repeated for $50\mu m$ pinhole.

damage.

- *With APD*: This part of the alignment is done after the incorporation and alignment of the APD (see next section). Less concentrated samples of $10nM$, $5nM$, $1nM$ and $0.1nM$ are prepared (in a chambered coverslip with 8 wells) and placed on the setup. The focus is set into the sample (as described in section 3.1.9). Next, the signal (cps) is checked and optimized systematically by adjusting the x-,y and z micrometer screw of the pinhole complex.

  Before and during the optimization of the signal by adjusting the position of the pinhole (by micrometer screws of the pinhole complex) one should routinely conduct measurements to see whether the correlation curve appears. If the alignment is more or less correct and the signal is optimized by APD then a correlation curve (most probably a bad one) "should" appear on the computer screen. However, getting the correlation curve proved to be very difficult in this case even though the alignment procedure was performed with care, caution and extreme precision. The root of this problem, which was ground loops (see discussion) was discovered later. However, it took approximately several months to get a correlation curve (see discussion). Once a correlation curve is obtained then the optimization process of the signal continues with regards to other components.

3.1.12 The detector

The detector is a critical component of FCS setups. Detectors used in this sort of setups can mainly be divided in two categories. Single point detectors e.g. avalanche photo-diode (APD) and photomultiplier tubes (PMT),

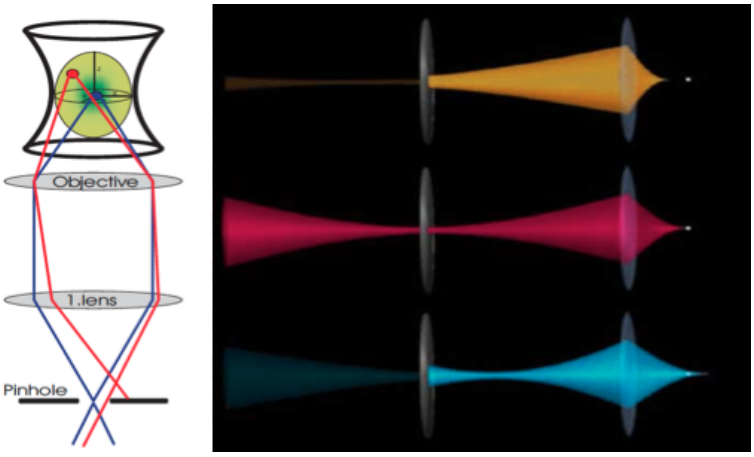

Figure 15: **Left**: Illustration the pinhole principle that facilitates the limitation of the detection volume in the direction of the propagation of the excitation beam. Light emerging from near the focal plane (blue spot) is collected and collimated by the objective and then focused by a second lens to pass through the pinhole and onto the APD. Light that originates from above or under the focal plane (e.g. red spot) is out of focus at the pinhole and only a small portion continues to the APD. The figure is from [20].
Right: The white spot illustrates the focal plane. The figure depicts three scenarios where light collection occurs respectively under-, at and above the focal plane. Top (yellow) and the bottom (blue) scenarios show inefficient collection of the fluorescent light (as light is collected below and above the focal plane), focused respectively to the left and the right of the conjugate image plane. Middle scenario (red) illustrates where light collection by the detector is efficient. Figure from (www.fcsxpert.com).

and imagining detectors e.g. electron multiplying charge coupled devices (EMCCDs). The latter type will not be discussed her.

A detector suitable for FCS measurements must fulfill some basic requirements necessary for conducting single molecule fluorescence experiments[24]:

- high quantum efficiency (QE) over the spectral range of the wavelengths of the light which are intended to be detected.

- a good linear tendency of quantum efficiency over the spectral range of the wavelengths of the light which are intended to be detected.
- sufficiently fast time response for the application
- low average dark count (i.e. low noise). The dark count of the APD used in this setup is $\sim 200 - 250$cps (at low excitation) depending on if it is pitch dark or partially dark (i.e. half closed curtains).

APD detectors are more commonly used compared to PMTs in single molecule fluorescence spectroscopy. APDs have normally higher quantum efficiencies in excess of 60% (compared to PMTs $\sim<$ 25% [21]), display good linearity and spectral response across the visible range mainly in the red part of the spectrum. PMTs on the other hand display poor linearity in output current intensities in this part of the spectrum [24]. However, PMTs are cheaper and have a larger active area $\sim mm^2$ compared to that of the APDs $\sim \mu m^2$ [27] [22], which means that the PMTs are easier to align and less vulnerable to photon induced degradation. However, The response time of the PMT is also shorter typically in order of $10's$ of picoseconds compared to the APDs $100's$ picoseconds [27].

The detector used in the FCS-setup described here is an APD (LASER COMPONENTS GmbH, SPCM-AQR-13). The reason for choosing APD as detector is partly the availability of two APDs in the lab. from the previous

[21] the QE of some newer models of PMTs are significantly higher e.g. Hamamatasu H7422-40P [26]

[22] This is perhaps not necessarily a negative quality. Since the small opening of the APD can be used as a pinhole blocking the out of focused light in different FCS optical arrangements.

setup and because APDs meet the above requirements quite well. Appendix C gives a detailed description of how an APD works.

Good FCS measurements require low-noise photon counting. The nature of photon-counting of a detector greatly affects the signal to noise ratio S/N.

Aligning the APD: Initially, efforts were made to incorporate two APDs in the setup. A polarising beam splitter (50 : 50) can be used to distribute the signal to both APDs. By using two APDs one can eliminate all the inherent noise from the APD's dark current as long as the detectors themselves are not correlated. Cross-correlation mode is applied to correlate the signal of one APD to signal of the other.

However, it turned out that one of the APD's do not work due to unknown defect. As mentioned before it is possible to conduct FCS experiments with only one APD (see the discussion section). It was therefor decided to use only one detector. By not using the beamsplitter and only using one APD, one actually effectively doubles the S/N ratio. The consequence is the loss of ability to record in cross-correlation mode which has a slightly better temporal resolution in the nanosecond range [18] (this issue will be discussed in more detail in the discussion section). Furthermore, the setup is intended for biological membrane diffusion measurements and this is below the needed temporal resolution for lipid lateral diffusion experiments, since fluctuations in this kind of samples occur on the millisecond timescale.

The APD is incorporated in the setup in the following way: First, the APD is connected to the correlator card (Flex5000/FAST[23]), which is con-

[23]Correlator.com, Bridgeeater/NJ,USA

nected to a computer.

- the vertical positioning of the APD is controlled by four screws to each corner of a metallic slab that the APD is attached to (see figure 6).

- the active area of the APD is covered with thick piece of cardboard paper (a cross hair is drawn on the cardboard paper), which is taped on the opening of the APD. This is done in order to protect the APD against incoming light and for alignment purposes. At this point (where the APD is covered) fluorescent light from a strong R6G sample is used for the alignment.

The active area of the APD is very small $176\mu m \times 176\mu m$. A $20mm$ lens L_5 (see figure 6) is used to focus the incoming fluorescent light exactly on the active area. Prior to the alignment of L_5 and the APD it is made sure that the light passes through the exact center of the L_5 lens and that the light beam hits the center of the cross hair (drawn on the cardboard paper attached to the APD opening). This is achieved by the help of precision pin in the same manner as for each of the other lenses.

- the L_5 lens is placed at such a distance, where its focal point corresponds to the center of the active area of the APD. The adjustments screws on the L_5-holder and its distance to the target is varied until the focus and the position of the light spot are satisfactory. This step is not very easy, since the focal point of L_5 is very short, and the intensity of the light spot is very weak.

Once the light path from the laser all the way to the APD is as well aligned as possible, it is time to optimize the signal by using a weak samples

of R6G. The target (i.e. cardborad paper) is removed and pipes are installed in order to block any stray- or other external ligth from getting to the APD.

3.1.13 Optimization

After the alignment of every component is done, and the dark count of the APD is checked. Weak samples of R6G (ranging from 10-0.1 nm) are prepared to be used for optimization of the signal. One should try to see if the correlation curve appears on the screen even before optimizing the signal (see figure 16).

However, the correlation curve proved to be very illusive. As mentioned before, the alignment of the entire setup was repeated multiple times. Every time at this stage the APD would start to behave erratic and unpredictable as the signal would typically increase drastically. It was discovered the dark count would also increase considerably after the electronic devices were turned on for approximately an hour or longer. This issue was solved by finding the source of the problem, which was the existence of ground loops (see the discussion section) and removing them.

After elimination of the ground loop-related noise problems, the optimization of the signal was done in the following manner:

The setup is optimized systematically in different steps:

- the fine tuning of the telescope by using the micrometer screw of the optical bench (i.e. the position of L_1) (see figure 6), while keeping an eye on the counts on the computer screen.

- optimizing the signal by fine adjusting the position of the pinhole re-

spectively in horizontal and vertical directions by using the micrometer screws of the pinhole stage (see figures 6 15)

- optimizing the signal by fine adjustments of the distance between L_5 and the active area of the APD. This is followed by systematically improving the signal by using the screws on the L_5 so that the fluorescence light spot hits the exact center of the active area.

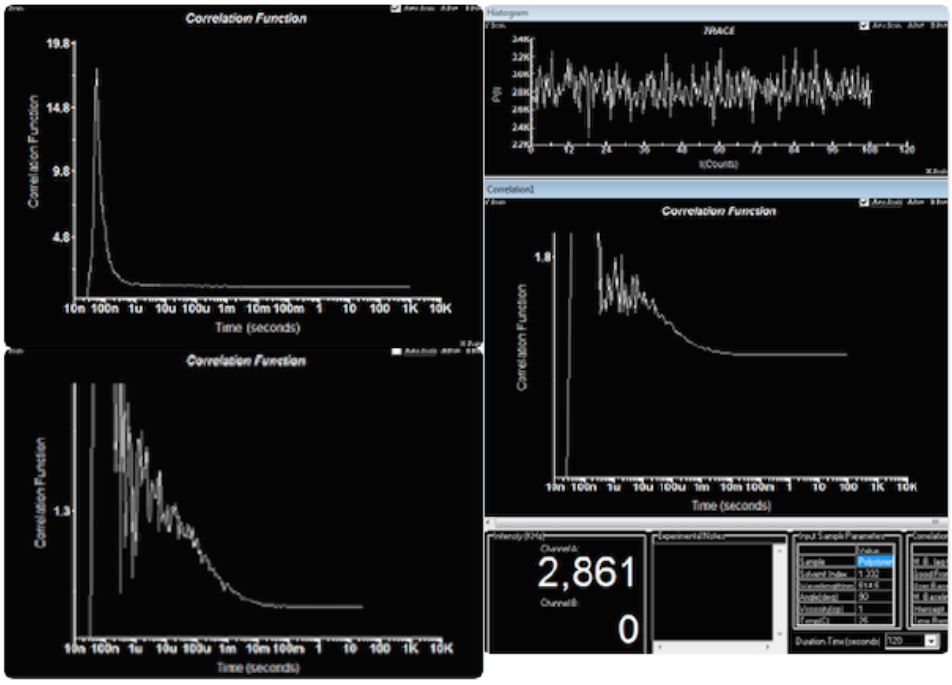

Figure 16: **left top**: no correlation curve is observed on the screen due to misalignment of the L_5 lens. **left bottom**: the correlation curve appears after slightly adjusting the distance of the L_5 lens relative to the active area of the APD. **Right**: an improved correlation curve after small adjustments of the pinhole.

During each of the three optimization steps mentioned above, one should systematically try to check whether obtaining the correlation curve (see fig-

ure 16) is possible. The detectable emission rate of a R6G fluorophore is approximately 1000kcps [17]. This means that a signal around a few 1000s kHz would be a good start. Once the correlation curve appears, one can try to improve it by further optimization of the pinhole and finding the right excitation intensity (i.e. the right OD).

It is worth to mention that after the construction- and optimization processes of the setup are complete. It is only necessary to optimize the signal by adjusting the pinhole and the distance of the objective to the sample during calibrations. One should not touch the other components unless there is misalignment in the light path.

The next step is to determine the size of the confocal volume. The size of the confocal volume (see figure 7) should be determined before experiments. The following section gives an explanation of how one can determine it.

3.2 Calibration

Prior to conducting FCS measurements it necessary to calibrate the setup. Diffusion time τ_D and number of particles N are the main parameters of interest in this kind of measurements. Both parameters are respectively related to the diffusion coefficient D_τ and the concentration C. In order to obtain the absolute values for the diffusion coefficient D_τ and the concentration C calibration is required since τ_D and N are both relative numbers strongly influenced by a number of experimental parameters as well as by each individual experimental setup. As discussed in the theory section both τ_D and N depend on the size of the detection volume. This indicates that calibration of FCS is all about determining the size of the observation volume. There

are several strategies for the determination of the detection volume. The following two approaches are probably the most common:

- measuring several different concentrations of fluorophores (e.g. R6G) followed by plotting N vs. C. The slope of the graph yields the detection volume.

- measuring a fluorophore aqueous solution where diffusion coefficient is known followed by curve fitting which yields τ_D and r_0 from which the confocal volume can be determined by calculation.

The latter method was applied in this project. the system was calibrated with $3nM$ R6G samples ($280\frac{\mu m^2}{s}$, $T = 296K$) in order to determine the radius of the detection volume.

In this context Rhodamine 6G molecules can be assumed as point like particles diffusing through the 3D detection volume (typically in order of $\backsim 300 - 600nm^2$) that is much larger than the individual R6G molecules ($\backsim 1.1 \times 1.5nm^2$) [14].

As discussed in the theory section the correlation function for the 3D diffusion of Rhodamine 6G molecules can be written as:

$$G(\tau)_{3D} = 1 + \frac{1}{\langle N \rangle} \cdot \left(\frac{1}{1 + \frac{\tau}{\tau_D}} \right) \cdot \left(\frac{1}{1 + \sqrt{1 + \frac{r_0^2 \cdot \tau}{z_0^2 \cdot \tau_D}}} \right) \tag{35}$$

The above equation has three fitting parameters, which are $\langle N \rangle$, τ_D and r_0^2. Since the diffusion coefficient of R6G is known, the number of fitting variables can be reduced to only two namely $\langle N \rangle$ and τ_D. Since D_τ is related

to r_0^2 through the following relation:

$$\tau_D = \frac{r_0^2}{4D_\tau} \tag{36}$$

substituting τ_D in $G(\tau)_{3D}$ yields:

$$G(\tau)_{3D} = 1 + \frac{1}{\langle N \rangle} \cdot \left(\frac{1}{1 + \frac{\tau}{\tau_D}} \right) \cdot \left(\frac{1}{\sqrt{1 + \frac{4D_\tau \tau}{z_0^2}}} \right) \tag{37}$$

The latter equation is used for fitting the data. τ_D and N are obtained from the fit and used for calculation of the confocal radius r_0. However, the confocal radious r_0 can vary by $\pm 50nm$ from time to time, but the most typical r_0 is around $390nm$. z_0 is estimated to be $2500 - 3000nm$ and not measured directly, and the ratio is $\frac{r_0}{z_0} = 5$. The autocorrelation functions in this thesis are fitted in OriginPro 2015.

4 Results

4.1 Determining the detection volume

The detection volume of the setup can be determined by conducting FCS measurements on a solution of known concentration of rhodamine 6G at $(298.15K)$. The correlation curve below is the result of FCS measurement of a $3nM$ rhodamine 6G aqueous solution.

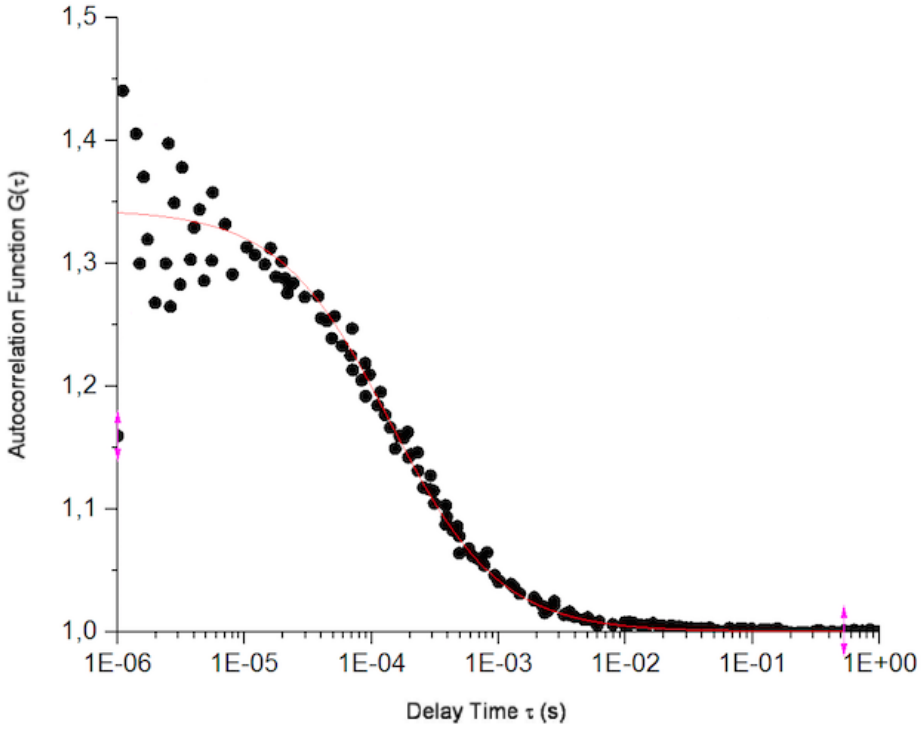

Figure 17: Autocorrelation function for a $3nM$ R6G aqueous solution ($OD1$, pinhole $100\mu m$).

The data are fitted with eq. 37 as described in section 3.2. The standard deviation of the measured values from the fitted values is ± 0.054. This shows

that the parameters obtained from the least-squares fitting are accurate. The fitted parameters obtained from the autocorrelation function were diffusion time $\tau_D = 1.4 \cdot 10^{-4} s$ and number of molecules $N = 3$. By using the the diffusion coefficient of R6G ($280 \frac{\mu m^2}{s}$), the radius of the confocal volume can be obtained by using eq. 36, which yields $r_0 = 396nm$. This gives us the axial length $z_0 = 1980nm$. Now the detection volume can be calculated by using $V_{det} = \pi^{3/2} r_0^2 z_0$, which yields $V_{det} = 1.728 \cdot 10^{-18} m^3$ i.e. $V_{det} = 1.73fl$. Now that the detection volume is known, one can calculate the concentration of the R6G sample (see eq. 20). Since,

$$\text{number of moles} = \frac{1mole \cdot N}{6.023 \cdot 10^{23}} \tag{38}$$

here, $6.023 \cdot 10^{23} \frac{1}{mole}$ is the avogadros constant.

$$C = \frac{\text{number of mole} \cdot 10^{-3} m^3}{V_{det}} \tag{39}$$

The above calculation yields $C = 2.9nM$, which agrees well with the actual concentration value of $3nM$.

4.2 Diffusion times and viscosity

In order to test the FCS setup, an experiment was conducted to see how the setup responds to variation of viscosities in aqueous R6G solutions at $298.15K$. The viscosity is varied by adding sucrose of different weight percentages $wt\%$ (see table below). The concentration of R6G is kept constant at $3nM$. $wt\% = 0$ means that no sucrose has been added.

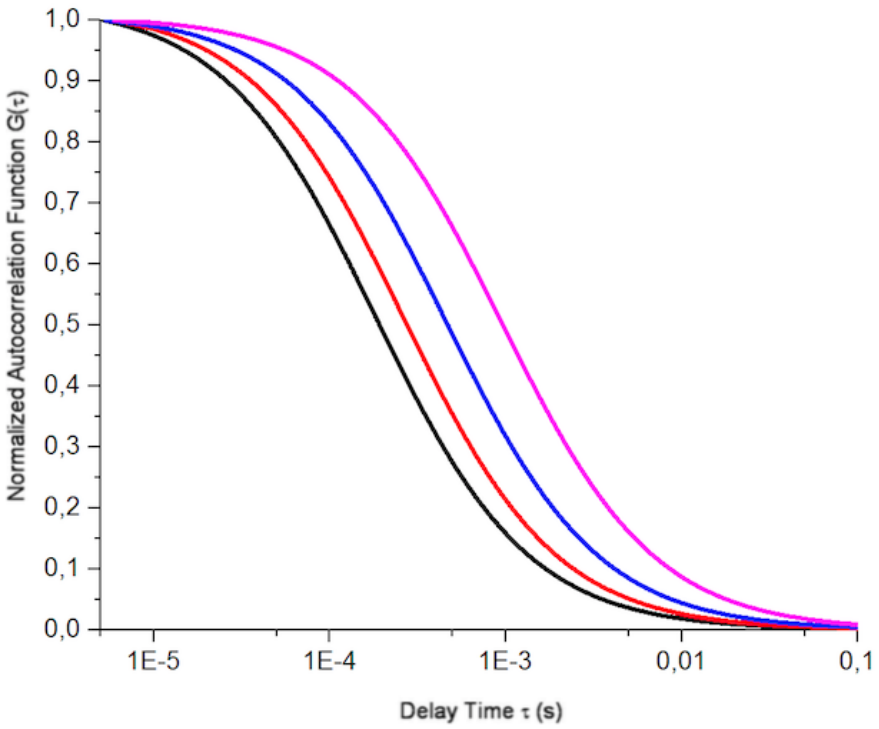

Figure 18: Normalized autocorrelation functions for different concentrations of sucrose solutions. Black $0wt\%$, red $10wt\%$, blue $20wt\%$ and magenta $30wt\%$

The autocorrelation functions of R6G ($3nM$) in sucrose aqueous solutions

Sucrose concentrations $(wt\%)$	0	10	20	30
Diffusion times μs (τ_D)	182 ± 14	264 ± 20	458 ± 45	954 ± 112
Diffusion constants $\frac{\mu m^2}{s}$ (D_τ)	280	192	110	52.8
Reported values viscosity $(mPa \cdot s)$	1.00	1.28	1.75	2.73

of different viscosities are fitted and the normalized autocorrelation functions are shown in figure 18. The graphs show that diffusion time τ_D increases as sucrose concentration is increased (see 19). The reported viscosity values for the different sucrose aquaous solutions (in distilled water, at $298.15K$)(see table above) are found in the literature [34, 35].

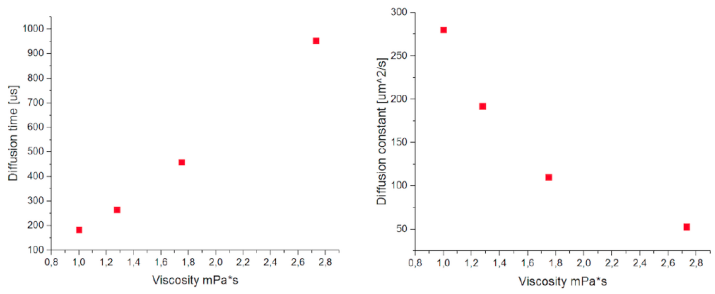

Figure 19: **Left**: shows the relationship between the varying viscosities and the diffusion times. **Right**: shows the relationship between the the varying viscosities and the diffusion constants.

As shown in the table above uncertainties of the measured diffusion times increases as viscosity is increased. At low viscosities the fluorophores move relatively fast, their motion is maintained in a dynamic equilibrium state. At higher viscosities the fluorophores move relatively slow. Hence, the state of dynamic equilibrium can not be kept, during the short measurement time of the fluorescence signal. The uncertainty of high viscosity solutions mea-

surements can be reduced by increasing the measurement time.

5 Discussion

In this section two important issues will be discussed. The first issue is the serious problem of ground loops that was encountered during the construction process. Here, some common causes that potentially lead to the creation of ground loops in our system will be discussed and possible solutions to the problem will be presented. The second issue is the difference between using one or two APDs. The difference between recording in auto- or cross correlation will be discussed. Furthermore, some light will be shed on advantages and disadvantages of using one or two APDs.

Undoubtedly, the most difficult challenge of this project was the identification and elimination of ground loops from the setup.

Ground Loop related problems can appear, and disappear just as unexpectedly as they appear in the first place. The root cause of these sort of noise-problems can often be extremely difficult to pinpoint, even by people who have extensive experience building experimental setups that include various electronic devices.

We initially expected, if the alignment process was correctly planned and executed, and the signal was well-optimized, then a correlation curve (probably even a bad one) "should" have appeared on the computer screen.

However, as mentioned earlier obtaining the correlation curve proved to be very difficult. Since after the completion of the alignment process, the APD started to behave unpredictably at times. As it would suddenly detect very large signals, that were sometimes several 1000s of times higher than expected.

This phenomenon was completely unknown to us. More than a dozen re-

constructions and realignments were therefore preformed on the setup. Furthermore, all the components of the setup were individually tested several times.

By the time, we were absolutely sure that all the individual components did not have any defects, and that our alignment- and optimization procedures were correct, we turned our attention to ground connections.

Ground connections are either created deliberately or totally unintentionally as a setup is constructed.

Unintentional- and uncontrollable ground connections can usually be created as instruments are mounted on the setup, cables are added and power leads are connected etc.

A serious consequence of these uncontrollable and unwanted ground topologies is, that voltage drop along a ground conductor in one section of the setup can result in spurious voltage drop in a totally unrelated section of the setup (or even some other place in the vicinity).

This can potentially cause the introduction of electrical noise in the system, which could alter the measurements, as well as other electronic problems in one or perhaps several electrical components of the setup. This phenomenon is often caused by "Ground loops" [33].

Ground loops become typically noticeable, when there are multiple pathways for signal and power supply currents to return to the power supply ground.

In these situations long cables can behave like "antennas", which can magnetically pick up low frequency electrical fields from the surroundings. Even fields generated by building wiring can (which for example carries power

to the fridge in the lab. or etc.) can be strong enough so that a ground loop can couple into your setup.

The word “grounding” is mentioned several times in this section. It is therefore important to emphasize that “proper grounding” in this case does not refer to establishing a proper electrical connection to the soil or rock surrounding the building.

In this case (i.e. the elimination of electrical noise due to ground loops), “grounding” also refers to the characteristics of the interconnections of the outer structure frameworks (i.e. chassis) of the devices, cables, a.c. mains ground conductors, and neighboring conducting objects (e.g. cable trays etc.).

In some cases it is not even necessary to establish contact with the ”earth” in order to avoid electromagnetic interference problems. It is perhaps not even helpful in some cases.

An airplane is a fine example to illustrate this point. Since airplanes consist of many electronic devices. These devices work together in a very electromagnetically noisy milieu without the possibility of establishing any contact with the ground.

Furthermore, contradictory to what most people might think, the mains a.c. safety grounds are not at the same voltage everywhere.

Due to an unbalanced inductive coupling between the current carrying power conductor and the ground conductor, net voltages may be induced on the ground conductor.

A configuration that displays such a phenomenon is sometimes called a “parasitic transformer” [33].

There is also the possibility of stray currents residing on the a.c. mains ground conductors. Theses stray currents can for example appear due to many different factors, such as current leakages from various electronic devices with damaged or inefficient insulation etc.

Voltage differences can arise between different points on the conductor (in this case different power outlets), due to the passage of stray currents along an a.c. mains safety-ground conductor, which has finite resistance.

Ground loops are an often-occurring problem as they are a notorious source of noise in setups that include sensitive electrical components.

In the two examples given below, ground loops can typically be a problem if the high-level analog or digital signals are being transmitted such long distances that the differences between the ground voltages at the transmitted and receiving ends up being unacceptably large.

Two simple and common scenarios involving ground loops are given below. In both examples, a measuring instrument is connected by shielded cables (grounded at both ends to their respective chassis) to a single or multiple signal source (e.g. APD, photomultiplier tube, camera etc.) that provides low-level voltage current information to be processed. Both devices are run by the a.c. mains, and the safety ground wires in their power cords also connect them with the common a.c. mains safety-ground through different power outlets in the lab. Both examples illustrate how an unwanted loop involving the shield connection of the signal links an unwanted time-dependent magnetic flux from some external source.

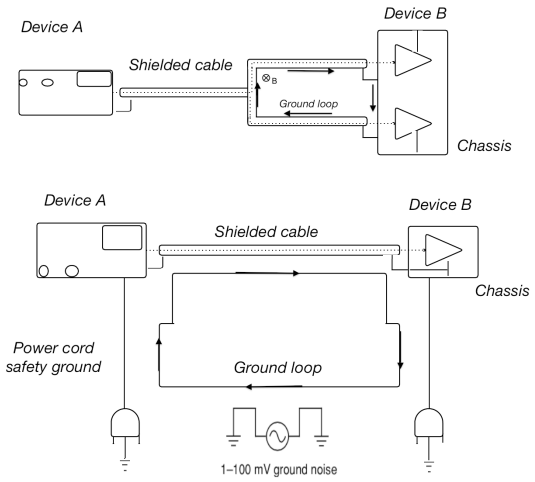

Figure 20: *Top*: Illustration of a ground loop in a bifurcated shielded cable. It shows unwanted current circulation in the area between the bifurcated branches due to the passage of stray a.c. magnetic fields through the enclosed loop. This current can result in a voltage drop along the cable, causing ground loop related noise at device B (e.g. a sensor). *Bottom*: Illustration of a ground loop in a.c. safety ground. The figure shows how noise voltages between power outlets facilitate the passage of current through the cable shield. This causes a voltage drop along the cable, which introduces ground loop related noise in the system (e.g. the amplifier).

Example I

Figure 20 bottom, shows an illustration of two electronic devices, which are connected by a shielded cable. The cable is grounded at both ends to the chassies of both of the devices. The devices are both powered by a. c. mains. Furthermore, they are connected to the common a. c. mains ground through different power outlets in the lab.

As mentioned above the a.c. main safety ground is not at the same voltage

everywhere. So as illustrated in figure 20 the presence of any leakage current and parasitic transformer will produce difference in ground voltage between the different power outlets.

Power outlet grounds on different walls of the lab. can actually differ from each other by several volts. This will cause the flow of the current through the cable shield, which connect device A and B.

This will in turn result in a voltage drop along the shield and ends up as noise in device B. This sort of noise voltages, which are caused by the different power outlets in the room (i.e. lab.) are usually $1 - 100mV$ of $50/60Hz$ line frequency voltages. Outlet grounds at different corners of a building can produce voltage differences of around $5V$ or even slightly higher [33].

Furthermore, there is also a high probability of the exsistence of considerable radio frequency noise as the a. c. mains conductor in the building tends to act as antennas.

Example II

Some setup arrangements do not include a. c. mains safety grounds, but still contain ground loops. These ground loops can pick up unwanted noise due to magnetic induction.

Figure 20 top, illustrates an example of this scenario where a shielded cable from device A branches out into two cables, so that the same signal is passed along into two different input channels of device B. The branched cables, together with the enclosure of device B can create a ground loop, which

result in circulating current caused by stray magnetic fields. This arrangement results in the appearances of noise voltages at both input channels. In experimental setups this type of ground loop related noise issue is typically less common compared to the noise problems related to a. c. mains safety grounds ground loop.

Actually, even when care is taken during the construction of the setup in order to avoid the creation of ground loops, they can still completely unexpectedly appear. There are though some "usual suspects" that can potentially result in the creation of ground loops. These problems are avoidable if one is careful during the construction process. A few typical suspects are listed below:

- plugging the electronic instruments of the same setup into different power outlets located at different positions (e.g. walls) in the lab. Furthermore, miswiring a. c. power plugs and receptacles can also lead to serious ground loop noise problems. For example if one mistakenly interchanges the neutral and the ground wires on plug or receptacle. This will cause power return currents from electronic devices amounting to many amps, which will pass through the safety ground network resulting in large voltages to appear in setups that have multiple contact to the safety ground. Tracking noise problems caused by this kind of miswiring can be very problematic, since setups relatively far away in different part of the building can be affected.

- the electronic instruments of the setup coming into unintended contact with each other while resting on the optical table.

- Using shielded cables that are worn out or damaged, which are in contact with for example grounded surfaces.

- coaxial cables coming into unintended physical contact (i.e. touching) with other parts of the setup such as electronic devices, grounded surfaces, optical table etc.

- existence of floating parts on the setup that are not being used as well as borrowing and reinstallation of parts of the setup especially electronic instruments or cables.

  So ground loops can be a serious reoccurring problem in laboratories, where some electronic devices are being shared by different experimental setups, and the devices are regularly installed and dismantled.

- sometimes subtle and innocent rearrangement of the wiring of the setup perhaps in order to minimize or eliminate noise problems can potentially cause the creation of ground loops. This could be a more serious problem in large and complex experimental setups that consist of many parts, where very small local changes to the wiring can have consequences for the entire setup.

Solving and avoiding ground loop related problems

While constructing an experimental setup, that includes electronic instruments, proper grounding of the setup should be kept in mind during the construction, and even planned before the setup is assembled (e.g. by drawing ground maps).

However, most leave the ground of setups to chance. This is of course not a good idea, since the risk of getting them in the system is much higher. Removing ground loops once they have manifested them selves through noise problems is a very complicated and tedious task.

The right approach would be considering the possibility of ground loops even before the construction process is initiated, and to plan for ground topologies.

It is always an advisable to use as few instruments and other parts as possible. Keeping things as simple as possible is a good strategy.

If an experimental setup already exists and is plagued by ground loop related problems, perhaps removing unused parts and devices would sufficient to eliminate any ground loops.

Here is a list of possible causes of ground loops, that were identified (or suspected) in our setup and how they were handled:

- keeping it simple: There were several electronic devices, other components and cables on and around the setup, which were not in use.

  These parts were removed and the setup was tested to see whether the problem was eliminated. Unfortunately, the problem still existed.

- keeping it neat: The maze of cables, that was formed during the construction process was sorted out. Furthermore, all the wires and cables that looked damaged were replaced with new ones.

  All the cables that were unnecessarily long were replaced with shorter ones to the extent possible. The cables were also separated so that they did not touch each other.

- single point grounding:

  The electronic devices were plugged into several different outlets (on different walls) in the laboratory. As previously mentioned this can potentially cause the formation of ground loops. It is a good idea not to make unnecessary ground connection. Luckily, removing these kinds ground loops can be done by implementing "single point grounding". Single point grounding is the most simple method for breaking and avoiding ground loops of this sort by only making ground contact at one point along a ground path. So all the electronic devices were plugged into one extension cord, which was plugged into the same power outlet. Furthermore, the optical table was also grounded at the same extension cord.

- Noise suppresion: In order to suppress possible high frequency noise in the system. We equipped most of the cables with EMI filters (i.e. ferrite beads).

All the above initiatives together broke the ground loop(s). The setup started to work normally immediately after the above mentioned corrections were implemented. We do not know for sure which of the steps described above or a combination of them eliminated the ground loop related noise, since all the steps excluding the first step were preformed simultaneously.

The second issue that needs some elaboration is how the system would function if two APDs instead of a single one were incorporated in the setup. As mentioned earlier due to a defect in one of our two APDs, we were not

able to incorporate both APDs in the setup as previously intended. Using only one APD has few advantages and some disadvantages, which will be discussed here.

Using two separate APDs make FCS more demanding from a technical perspective. One of the main advantages of using one instead of two APDs is the much easier alignment due to not using a beamsplitter and an extra APD. Furthermore, not using a beamsplitter (50 : 50) and only using one APD effectively doubles the S/N ratio.

However, using one APD limits us to only being able to record in auto-correlation mode. Since auto-correlation mode uses the signal from only one APD at time t and correlates it with the single from the same APD at a later time $t + \tau$. The disadvantage of recording in auto-correlation modes is the presence of many more electronic artifacts on fast time scale as opposed to cross-correlation.

These electronic artifacts may cause deviations in measured values. Two of the most common detector nonidealities, that cause these artifacts are detector dead time and afterpulsing.

Detector dead time is a result of minimum recovery time after each event, where the detector is unable to detect the next photon after a previous photon detection [28]. Typically, detector dead times are in order of tens- to hundreds of nanoseconds ($30ns$ for our APD). Detector dead times cause a drop of the measured ACF towards zero at lag times of the order of the detector dead time. Since usually this time region is not of interest in FCS measurements it will not be discussed any further here.

However, a major nonideality of the detectors (i.e. APD in this case) is

that they generate afterpulses, which cause the appearance of large peaks just before the correlation curve begins (see figures 21 and 16).

Afterpulses are the generation of spurious photon detections as response to actual detection event shortly after a genuine photon detection event has taken place [28]. There is a probability that each "real" signal is followed by an afterpulse at a later time.

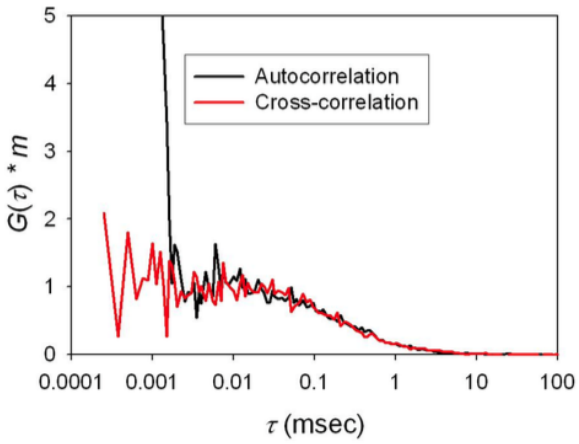

Figure 21: An illustration of the difference between recording in aut- and cross-correlation. The two correlation curves are from the same sample (fluorescently-labeled protein) recorded in auto- and cross-correlation. This figure is adopted from [32].

These afterpulses are highly correlated to the initial occurrence and result in a large background noise in the FCS curve causing a peak in the acquired correlation curve on a short time scale as previously mentioned. The problem is that they can "mask" some information that the curve might contains in short lag times. For example, it can lead to difficulties in determining a very exact average number of molecules in the detection volume along with their diffusion constants.

The origin and characteristic of afterpulsing depend on the nature of the detector and the working environment[31].

It is worth to mention that today new hybrid photon detectors are commercially available. These detectors show very low even no afterpulsing [24] (model H8236-07 from Hammamatsu Corp., Bridgewater, New Jersey is a good example).

The elimination of the afterpulsing signal can be achieved by applying several methods. These methods includes for example filthering based on fluorophore life times or truncation of the correlation curve [28].

However, a widely used and effective solution for diminishing the impact of APD afterpulsing on an ACF is to incorporate two separate detectors in two detection channels [31]. A beamsplitter $(50:50)$ can be inserted on the emission pathway (see figure 6), which divides the emission signal into two and directs it towards both APDs.

This makes it possible to approximate the ACF by cross-correlation of the signals between the two detectors instead of auto-correlating each detector signal. This is possible since afterpulses of one of the detectors is completely uncorrelated to real photon detection events of the second detector.

To record in cross-correlation mode basically means that the signal from one APD, which detects the parallel emission signal at time t is correlated with the signal from the other APD, which detects the prependicular emission signal at time $t + \tau$.

However, splitting the flourescence light results in the reduction of number of counts at each APD. This can lead to an increase in fluctuations, which

[24]The payoff is that some of these models have lower quantum effiencies compared to the main stream detectors.

in turn requires longer time for data collection.

As discussed above and shown in figure 21, cross-correlation mode has a somewhat better temporal resolution in the nanosecond range. So if one wants to conduct experiment on for example lipid membranes, using one APD should suffice. Since this is far below the needed temporal resolution for lipid lateral diffusion experiments where fluctuations typically occur in the millisecond timescale [18]. This is also supported by our experiment (see section 4.2), where we demonstrated that the setup is able to conduct in the required timescales. Furthermore, the earlier FCS setup constructed from almost the exact same components (except the $5mm$ lens and the cleanup filter) was able to preform well on lipid membranes using only one APD [18].

6 Conclusion and outlook

The aim of this study was to build a FCS setup, and document the construction process in a way that this thesis can serve as a "guide" for future FCS-construction- or realignment processes. The setup was constructed mostly from optical components and parts that were already available in the laboratory (from previous setups), with the exception of a few newly purchased parts (a $5mm$ lens with a nanobench and a cleanup filter $542 - 642nm$).

After careful calculations and considerations of the suitability of every component of the setup, the construction process was initiated by mounting every compnent on its precalculated/predecided position on the optical table. The alignment of the light began at the excitation source i.e. the laser ($532nm$ Nd:YAG, $5mW$). The laser beam was expanded by the telescope consisting of a $5mm$- and a $100mm$ quartz lenses. The telescope expands (and collimates) the beam $20\times$ to $7.2mm$ slightly overfilling the back of the microscope objective ($60\times$W, NA 1.20 and WD $0.25\mu m$). The microscope objective focuses the excitation light into the sample creating a detection volume of $\backsim 1,7fl$. The objective then collects the flourescence light from the sample at the detection volume. A bandpass filter (transmission $542 - 622nm$) was positioned to discriminate against unwanted contribution of the water molecules in the sample to the background noise. A lens-pinhole-lens ($100\mu m$, $50\mu m$ $30\mu m$) complex was constructed, since confocal detection scheme requires a narrow pinhole in the optical detection path.

The collected fluorescence light by the objective is focused onto the pinhole in a way that only light collected from very close to the focal plane of the objective is transmitted through the pinhole. So the pinhole functions

as a 'spatial-filter', as its purpose is to define as close to a near-Gaussian profile as technically possible. The pinhole is of course an extremely important element of the setup as it defines the confocal volume and prevents the unwanted artifacts from reaching the detector.

The detector used in the setup is an APD. Initially it was decided to use two APDs, but due to a defect in one of our two APDs, we were not able to incorporate both APDs in the setup. Using a single APD means the loss of ability to record in crosscorrelation mode and the introduction of afterpulsing in the data. Cross-correlation mode has a slightly better temporal resolution in the nanosecond range. Since the setup is eventually intended to be used for conducting experiment on lipid membranes, using one APD should suffice. It should be noted that this is far below the needed temporal resolution for lipid lateral diffusion experiments, where fluctuations typically occur in the millisecond timescale.

The system was optimized by making fine adjustments to the telescope, the position of the pinhole and the APD lens until a correlation curve was obtained.

However, we were not initially able to record a correlation curve. The construction- and realignment process were therefore repeated many times and every component was individually checked. During this process it was discovered that the system was severely affected by ground loop related noise problems. The root cause of ground loop related noise in a system can often be extremely difficult to pinpoint. Thus, the most difficult challenge of this project was the identification and elimination of ground loops from the setup. The ground loops were eliminated by mainly by single point grounding and

electromagnetic noise suppression.

An experiment was conducted to test the precision of the FCS setup. The results showed that the setup responds accordingly to variations in viscosity in aqueous R6G solutions.

The setup can be even further optimized in order to reduce the detection volume closer to $1fl$ mainly at the pinhole and the telescope. This will presumably result in a more sensitive setup, which would provide more exact measurements.

Presently, the setup does not include a CCD camera or any other form of binocular observation of the sample. Incorporation of a CCD camera can be used for supplementary microscopy studies of the sample. Since we already have a functional FCS setup, implementation of a camera should be relatively simple from a technical point of view.

Furthermore, an extra APD can be included in the setup by simply placing a polarising beam splitter in the emission pathway after the pinhole. This will result in the elimination of the afterpulses in the recorded signal. The removal of afterpulsing should also enable the system to preform experiments that require shorter time scales.

Appendix A: FCS procedure

- Clean and drying the sample "holder" e.g. chambered coverglass, cuvette etc.

- Remove air bubbles (after transfering the sample to e.g. chambered coverglas) and resting the sample for some time (depending on which kind of a sample it is) in order to ensure homogeneity of the fluorescent particles in the sample. For R6G rest for approximately 10-20 minutes in order for the particles to adsorb to the walls of e.g. chambered cuvette inner surface and allowing possible turbulence to calm. Furthermore, during this periode the temperature of the sample will also reach room temperature.

- Place a drop of distilled water on the objective. If the water drop stays on the objective for a long time, it will evaporate due to heat. This can of course effect the light collection efficiency, which would decrease as the drop evaporates. Replacing the drop is a possibility,but it might alter the measurements. Since one would has to remove the sample from the stage, put it back on and place the focus back in the sample.

- Place the sample inside the sample by using the flip-mirror, while making sure that the focus is not near (above) the coverglass. Thereafter, maximizing the signal by further minor adjustment of the distance between the objective and the sample.

- Optimize the counts by adjusting the pinhole.

- Determine the radius of the radius by recording correlation curves of a R6G sample .

  Different OD-filter yields slightly different correlation curves and therefor also varying different τ_D resulting in different different confocal radii. It is worth recommending that the calibration prior to conducting experiments should be performed using different OD filters. Since using a different filter(s) than the one used for calibration would probably result in inaccurate data.

- Save the newly found focal radius and use it in the planned experiment(s) of the day.

Appendix B: Components

This section provides a more detailed descriptions of some of the key components which are used in the setup.

Part	**Description**
Laser	532nm green, Nd:YAG, max output 50mW, beam diameter 0.36mm, TEM_{00} mode, LASER2000, Reno/NV USA
OD	five neutral filter options OD 3, 2, 1, 0.1, 0.6, 0, OWIS Staufen, Germany
L1	5mm focal lenght,quartz lens, Linos, Goettingen Germany.
L2	100mm focal lenght,quartz lens, Linos, Goettingen Germany.
Dich. mirror	Cutoff 537nm, AHF Germany
Objective	UPLAPO 60XW, NA 1.20, WD 0.25μm, FN 26.5, CC $0.31 - 0.21\mu$m, objective focal length 3mm, Olympus Optical Com, Hamburg Germany.
Filter	Transmission $542 - 622$nm, AHF analysentechnik AG, Tubingen Germany.
L3	140mm quartz lens, Linos, Goettingen Germany.
Pinhole	Rotating disk with pinhole options 100μm, 50μm and 25μm
L4	140mm quartz lens, Linos, Goettingen Germany.
L5	20mm quartz lens, Linos, Goettingen Germany.
APD	LASER COMPONENTS GmbH, SPMC-AQR-13, Olchin Germany
Correlator card	FLEX5000/FAST, CORRELATOR.COM, Bridge Water USA.

Appendix C: How does an Avalanch Photodiode (APD) work?

Avalanche photodiodes (APD) are highly sensitive and high speed semiconductor light detectors. Compare to regular PIN photodiodes, where an incoming photon produces only one electron- hole pair, APDs have an internal region in which electron multiplication takes place. APDs are basically photodetectors with a built-in first stage of gain through avalance mulitplication. By the application of high external reverese bias voltage, APDs show an internal gain effect due to the avalanche effect (i.e. impact ionization).

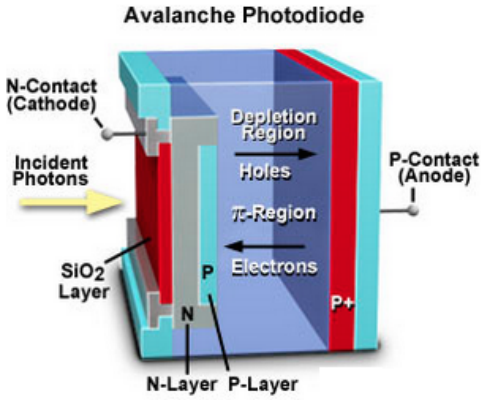

Figure 22: An illustration of the anatomy of an APD. The figure is from hamamatsu.magnet.fsu.edu/articles/avalanche.html

Most commonly available APDs are made from silicon, and have the so called reach-through structure. The figure above show the anatomy of a typical APD. An incident photon enters through the silicon side. As seen in the figure above, a positive p^+-region and a negatively doped N^+-region confine the depletion region (or π-region). The depletion region can also be

referred to as the absorption region, since the photons are absorbed here. This results in the generation of free electron-hole pairs in the depletion region. Furthermore, between the π-region and the N^+-region, there is a lightly doped p-type material called the p-region.

The APD is reversely biased, which indicates that it has the anode contact (N-contact (+)) on the N^+-region and the cathode contact on the (P-contact (-)) on the p^+-region. The region between the p-n junction is the avalache region, where the electric field is larger due to the fact that a large part of the reversed bias (see figure 23 left) is dropped across this region.

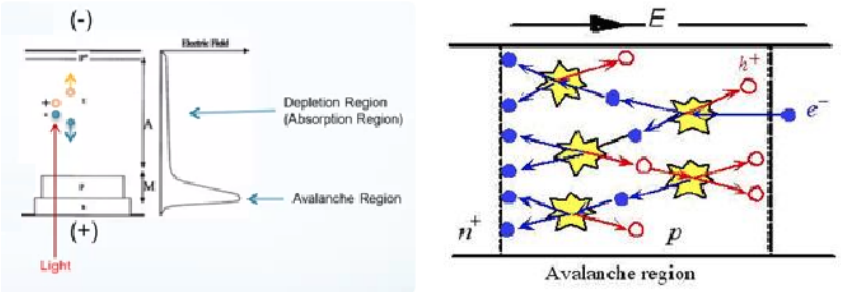

Figure 23: **Left**: A schematic illustration of the avalanche process in APD. **Right**: An illustration of the avalanche region (p-region). The figure is from

As seen in the figure above the photons enters through the N^+- and the p-region, and are absorbed in the π-region. This generates a free electron-hole pair in the π-region. Influenced by the electrical field in the absorption region the negatively charged electron wanders towards the anode (the avalanche region), while the positively charged hole goes towards the cathode p^+-region. Nothing further happen to the hole since the p^+-region does not include an avalanche region, as apposed to the electron that enter the p-region where it experiences the high electric field (see figure 23 left) and is accelerated and

encounters atoms (see figure 23 right). At this region the field accelerates the electrons to such a high speed that it creates more electron-hole pairs through collisions. This is referred to as impact ionization. The electrons and holes are then accelerated and thereby generate even more electrons and hole which repeat the process. This is referred to as the avalanche effect.

References

[1] Schwille, P.; Haustein, E., *Fluorescence Correlation Spectroscopy: An Introduction to its Concepts and Applications.*,Biophysics Textbook Online (BTOL),2002

[2] J.R. Lakowicz, *A Document Preparation System.* Addison Wesley, Massachusetts, 2nd Edition, 1994.

[3] R. Cotterill, *Biophysics an Introduction.*. Chichester, West Sussex New York: John Wiley, 2002

[4] A. Fick, *Ueber Diffusion.* Annalen Physik und Chemie 170(1),p. 59-86, 1855.

[5] A. Einstein, *The motion of elements suspended in static liquids as claimed in the molecular kinetic theory of heat.*. Annalen Der Physik 17(8): 549-560. 1905.

[6] Magde, D., Elson, E. L., Webb, W. W., *Thermodynamic fluctuations in a reacting system: Measurement by fluorescence correlation spectroscopy.* Phys Rev Lett, 29, 705–708., 1972.

[7] Elson E.L., Magde D, *Fluorecsence Correlation Spectroscopy I. Conceptual Basis and Theory*,Biopolymers, 13, pp. 1–27, 1974.

[8] Elson E.L., Magde D,Web W. W. *Fluorescence correlation spectroscopy II. An experimental realization*,Biopolymers, 13, 29–61. 1974

[9] Ehrenberg, M., Rigler, R., *R. Rotational brownian motion and fluorescence intensity fluctuations*, Chem Phys, 4, 390–401, 1974.

[10] Rigler, R, U. Mets1, J. Widengren and P., *Fluorescence correlation spectroscopy with high count rate and low background: analysis of translational diffusion.*, European Biophysics Journal 22(3), 159, 1993.

[11] Wiener N., *Extrapolation, Interpolation, and Smoothing of Stationary Time Series*, The Technology Press of The Massacgusetts Institute of Technology andWiley, New York, 1950.

[12] Hess S.T., Shaohui H., Heikal A.A., Webb W.W. , *Biological and Chemical Applications of Fluorescence Correlation Spectroscopy:*,A Review. Biochemistry, 41, pp. 697–706, 2002.

[13] Hess S.T., Shaohui H., Heikal A.A., Webb W.W. , *Focal Volume Optics and Experimental Artifacts in Confocal Fluorescence Spectroscopy.*,Biophys. J., 83, pp. 2300–2317, 2002.

[14] Kievsky YY, Carey B, Naik S, Mangan N, ben-Avraham D, *Dynamics of molecular diffusion of rhodamine 6G in silica nanochannels*,J Chem Phys 128: 151102, 2008.

[15] Madge D, Elson E, Webb WW., *Thermodynamic fluctuations in a reacting system – Measurement by fluorescence correlation spectroscopy.*,Phys. Rev. Lett. 29,705–708, 1972.

[16] Eggeling C., Widengren J., Rigler R., Seidel C. *Photobleaching of Fluorescent Dyes under Conditions Used for Single-Molecule Detection: Evidence of Two-Step Photolysis.*,Anal. Chem., 70, pp. 2651–2659, 1998.

[17] Hac, A. *Diffusion process in membranes containing coexisting domains investigated by fluorescence correlation spectroscopy.*, Gottingen, Copenhagen, Max Planck Institute (Gottingen), Niels Bohr Institute (University of Copenhagen). Ph.D. Thesis, 2003.

[18] Hac, A. *Phase Behavior and Enzyme Dynamics at the Lipid-Water Interface - a monolayer, fluorescence microscopy, and spectroscopy study* Copenhagen, Niels Bohr Institute (University of Copenhagen). Ph.D. Thesis, 2008.

[19] Blicher, Andreas. *Permeability studies of lipid vesicles by Fluorescence Correlation Spectroscopy and Monte Carlo simulations* Copenhagen, Niels Bohr Institute (University of Copenhagen). Master Thesis. 2007.

[20] A. Rosengren and P. B. Jensen. *Investigating the motility of E.coli using Fluorescence Correlation Spectroscopy* Copenhagen, Niels Bohr Institute (University of Copenhagen). Bsc. Thesis. 2005.

[21] Hac, A. E., H. M. Seeger, et al. *"Diffusion in two-component lipid membranes - A fluorescence correlation spectroscopy and Monte Carlo simulation study."*,Biophysical Journal 88(1): 317-333., 2005.

[22] Bockmann, R. A., A. Hac, et al. *"Effect of sodium chloride on a lipid bilayer."* ,Biophysical Journal 85(3): 1647-1655., 2003.

[23] Koppel, D. *Statistical accuracy in fluorescence correlation spectroscopy*, Physical Review Letters: A, 10(6), 1938-45., 1974.

[24] Gell C, Brockwell D, and Smith A; *Hand book of single molecule fluorescence spectroscopy;*, Oxford Univ. Press. 2006

[25] Rhoades E, Gussakovsky E, and Haran, G. *Watching proteins fold one molecule at a time.*, Proceedings of the National Academy of Sciences of the United States of America 100, 3197–3202. 2003

[26] Becker W. *Advanced time-correlated single photon counting techniques*, Springer, New York. 2006

[27] Geddes D. Chris. *Reviews in flourescence 2009*, Volume 6, Springer, New York. 2011

[28] Enderlein, J. and I. Gregor (2005). *Using fluorescence lifetime for discriminating detector afterpulsing in fluorescence-correlation spectroscopy.*, Rev. Sci. Insrum. 76(3): 033102 - 033102-5. (DOI: 10.1063/1.1863399) 2005.

[29] Woll Dominic. *Fluorescence Correlation Spectroscopy in Polymer Science*, Volume 4, Issue 5, p. 2447-2465, Royal Society of Chemistry. 2014

[30] Jaeran Lee, Yumi Lee and Sok Won Kim. *Measurement of the Diffusion Coefficients of Single Molecules by Using Fluorescence Correlation Spectroscopy with a Software Correlator*, Journal of the Korean Physical Society, Vol. 59, No. 5, pp. 3171-3176 2011.

[31] Zhao, M., L. Jin, et. al. *Afterpulsing and its correction in fluorescence correlation spectroscopy experiments.*, Appl. Optics. 42(19): 4031-4036. (PMID: 12868844) 2003.

[32] Anderson, Val. *Principle factors influencing the accuracy of FCS data*, Cornell University, Application note 3.

[33] Walker, I. R. *Reliability in scientific research: improving the dependability of measurements, calculations, equipment, and software*,Cambridge University Press. 2011.

[34] M. Bourne. *Food Texture and Viscosity: Concept and Measurement*, Academic Press, California, , p. 78. 2002.

[35] M. Mathlouthi and P. Reiser. *Sucrose Properties and Applications* , Blackie A& P, London, p. 137. 1995.